Science Advances
AAAS

Supplementary Materials for

Characterizing many-body dynamics with projected ensembles on a superconducting quantum processor

Zhiguang Yan *et al.*

Corresponding author: Zhiguang Yan, marzgy09@gmail.com; Zi-Yong Ge, ziyong.ge@riken.jp

Sci. Adv. **12**, eaeb8213 (2026)
DOI: 10.1126/sciadv.aeb8213

The PDF file includes:

Supplementary Text S1 to S7
Table S1
Figs. S1 to S21
Legend for movie S1
Legend for file S1
References

Other Supplementary Material for this manuscript includes the following:

Movie S1
File S1

S1 Experimental wiring setup

The measurement setup for our superconducting qubit system is illustrated in Fig. S1. The sample is housed within a Blufors LD400 dilution refrigerator, which maintains a base temperature of approximately 10 mK at the mixing-chamber (MC) stage. For each unit consisting of four qubits and one readout port, we employ a near-quantum-limited impedance-matched parametric amplifier (IMPA) (*54*) to amplify the readout signals at the MC stage, achieving an amplitude gain of around 20 dB with a 600–700 MHz bandwidth.

A DC source (Yokogawa GS200) is utilized to apply the DC coil current to flux-bias the IMPA at its operation frequency. As shown in Fig. S1, twisted-pair DC cables are used in the flux-bias line to mitigate the electric and magnetic noise from the environment. In addition, to suppress the high-frequency noise, a π-filter (cutoff ~ 1 MHz) at room temperature and a homemade RC filter (cutoff ~ 2 kHz) at the 4 K plate are implemented. In the setup, a frequency doubler (Marki ADA-1030) is used to generate the high-frequency pump signal for the IMPA, which ranges from 16.2 to 16.9 GHz, approximately at twice the readout-resonator frequency. The long-time readout results shown in Fig. S15 indicate that the DC source and the frequency doubler remained stable during the experiments.

In our setup, the quantum analyzer (Zurich Instruments UHFQA) is used to generate the readout input (RIN) signals and demodulate the readout output (RO) signals. As shown in Fig. S3B, four readout resonators are coupled to a single readout port in one unit on our chip, allowing us to perform frequency-multiplexed readout through the four readout resonators. To ensure that the local-oscillator (LO) signals for the modulation and demodulation are phase-locked, we employ a Keysight microwave source to generate the LO signal, which is then amplified and goes through a power splitter to produce two phase-locked LO signals: one for the modulation and the other for the demodulation. The Zurich Instruments HDAWG8, an arbitrary waveform generator (AWG), generates all XY and Z control signals for the tunable transmon qubits (*28*). As depicted in Fig. S1, we utilize two AWG ports to generate the in-phase (I) and quadrature (Q) signals, which are then multiplexed with a LO signal by an IQ Mixer (Marki MMIQ-0218L) to produce the drive

signal for the qubit. The HDAWG8 supports DC settings, allowing us to generate the DC and fast Z-pulse from a single output port. We combine the XY and Z signals at room temperature through a diplexer (QMC-CRYODPLX-0218). Then, the combined signals are sent to the qubit through microwave cables in the refrigerator. Using this approach, we can fully control each qubit with just one microwave coaxial cable.

In the experiment, we require both low-frequency and high-frequency signals, which are used respectively to modulate the transmon qubit frequency and to drive the qubit transition. For the DC signal, we do not want it to be attenuated at the MC stage to avoid generating heat which might be transferred to the qubit and/or lead to a temperature increase of the MC plate. On the other hand, for the high-frequency drive signal, it is essential to be attenuated at the MC stage to suppress the high-frequency noise coming from the high-temperature plates. To address this issue, we developed a special low-pass filter. As shown in Fig. S2, it features a 2 GHz passband for the low-frequency flux-bias signal and a relatively flat passband (4.5–6 GHz) with an attenuation of approximately 10 dB for the high-frequency drive signal. In developing this low-pass filter, three key considerations were taken into account:

1. **Sufficient attenuation at the qubit frequency**: The filter must provide enough attenuation at the qubit frequency to suppress the qubit thermal excitations.

2. **Flat response in the frequency domain**: It is essential to maintain a flat frequency response within the range of the qubit frequency. It is critical for the waveforms of the qubit drive signal, particularly for the short-time pumping signals. As shorter signals have larger bandwidths, excessive variations in attenuation across the frequency range would significantly distort the signals in the time domain.

3. **Thermal contact to the MC plate**: Ensuring good thermal contact between the low-pass filter and the MC plate. Poor thermal contact could result in the filter's temperature exceeding that of the MC plate, allowing high-temperature noise to reach the qubit.

In our wiring setup, we maintained two different wiring configurations for qubit control: the

drive lines for Q_3, Q_7, Q_8, Q_9, Q_{12} and Q_{13} are designated as XYZ1 and the other lines are designated as XYZ2. The qubits connected to the drive lines XYZ1, even with the total attenuation 10 dB less than that in the drive lines XYZ2, showed comparable thermal population and T_1 (see Table S1 and Figs. S5D and S5E). The observed variations in the qubit thermal population may arise from the attenuation variations in the low-pass filter. In particular, Q_9 with the XYZ1 wiring configuration and the total attenuation of only 22 dB exhibits a thermal population of 0.66% and $T_1 \approx 50$ μs at the frequency of 5715 MHz.

S2 Device design

Our experiments are conducted on a scalable, two-dimensional superconducting quantum processor and enables full qubit control (Z- and XY-control). All the control signals access the quantum processor via spring contacts vertical coaxial-cable wiring. As depicted in Fig. S3A, the 4×4 tunable transmon qubit chip is mounted onto a stage featuring a 2D spring-contact array, aligned with the corner pillars. Figure S3D presents the cross-section along the dashed line in Fig. S3A. All the spring contacts directly contact the backside of the chip. The Z/XY-control pin is connected to the back end of the qubit, with the contact point (green) shown in Fig. S3C. Each readout pin is connected to a readout superconducting through-silicon via (TSV; yellow-green), which couples capacitively to the $\lambda/4$ band-pass filter (purple) on the top side of the chip, functioning as a transmission line.

As shown in Fig. S3B, each $\lambda/4$ band-pass filter couples to four readout resonators (light blue), allowing frequency-multiplexed readout for each unit consisting of four qubits. In addition, numerous TSVs are placed in the chip, connecting the segmented topside grounds to the backside ground to suppress potential slot-line or substrate modes. Moreover, these TSVs help to localize the control signals, reducing unwanted crosstalk. In our case, we achieved X-crosstalk below 1×10^{-3} and Z-crosstalk below 5×10^{-3} between any control port i and qubit Q_j ($i \neq j$).

As shown in Fig. S3B, we implement floating tunable transmon qubits (light gray) with concentric geometry optimized through the surface-participation-ratio analysis (*50*). The loop size of

our concentric qubit is approximately 3×10^5 μm^2, nearly three orders of magnitude larger than typical SQUID loops used for qubits. However, as illustrated in Fig. S4B, with the gradiometric geometry and optimized linewidth in the qubit design, the square-root amplitude $\sqrt{A_\Phi}$ of the $1/f$ flux noise spectral density A_Φ/ω is about 4.9 $\mu\Phi_0$, which is comparable to those in conventional designs (*55*).

To couple adjacent qubits, a coupler bus (dark red) is employed. The Hamiltonian for two adjacent qubits, Q_i and Q_j, along with the coupler bus, is given by

$$\hat{H}/\hbar = \omega_i \hat{\sigma}_i^+ \hat{\sigma}_i^- + \omega_j \hat{\sigma}_j^+ \hat{\sigma}_j^- + \frac{1}{2}\omega_c \hat{a}^+ \hat{a} + g_j(\hat{\sigma}_j^+ \hat{a} + \hat{\sigma}_j^- \hat{a}^\dagger) + g_i(\hat{\sigma}_i^+ \hat{a} + \hat{\sigma}_i^- \hat{a}^\dagger) + g_{ij}(\hat{\sigma}_i^+ \hat{\sigma}_j^- + \hat{\sigma}_i^- \hat{\sigma}_j^+). \tag{S1}$$

Here, ω_i, ω_j, and ω_c denote the frequencies of Q_i, Q_j and the coupler, respectively; g_i (g_j) represents the coupling strength between Q_i (Q_j) and the coupler. The parameter g_{ij} denotes the direct coupling strength between two nearest-neighbor qubits. The operators $\hat{\sigma}^\alpha$ ($\alpha = x, y, z$ and $\hat{\sigma}^\pm = \hat{\sigma}_j^x \pm \hat{\sigma}_j^y$) correspond to the Pauli matrices of qubits, while $\hat{a}$ and $\hat{a}^\dagger$ represent the lowering and raising operators of the coupler mode. By applying the Schrieffer–Wolff transformation (*56*),

$$\hat{U} = \exp\left[\sum_{\lambda=i,j} \frac{g_\lambda}{\Delta_\lambda}\left(\hat{\sigma}_\lambda^+ \hat{a} + \hat{\sigma}_\lambda^- \hat{a}^\dagger\right)\right]. \tag{S2}$$

The coupler can be effectively decoupled from the system up to second order in g_λ/Δ_λ, yielding an effective XY model

$$\hat{H}_{\text{eff}}/\hbar = \sum_{\lambda=i,j} \tilde{\omega}_\lambda \hat{\sigma}_\lambda^+ \hat{\sigma}_\lambda^- + \left(\frac{g_i g_j}{\Delta} + g_{ij}\right)(\hat{\sigma}_i^+ \hat{\sigma}_j^- + \hat{\sigma}_i^- \hat{\sigma}_j^+). \tag{S3}$$

Here, the coupler is assumed to remain in its ground state, which holds true in our experiment. $\Delta_\lambda = \omega_\lambda - \omega_c$ is the frequency detuning between qubit Q_λ and the coupler. The parameter Δ, defined as $1/\Delta = (1/\Delta_i + 1/\Delta_j)/2$, represents the effective detuning. $\tilde{\omega}_\lambda = \omega_\lambda + \left(g_\lambda^2/\Delta_\lambda\right)[\alpha_\lambda/(\Delta_\lambda + \alpha_\lambda)]$ is the Lamb-shifted qubit frequency, where α_λ represents the anharmonicity of Q_λ. In our device, the frequency of the coupler buses used to connect adjacent qubits within a unit is about 22 GHz, while the frequency of the coupler buses used to connect adjacent qubits between neighboring units is approximately 40 GHz. The considerable detuning between the qubit and the coupler bus

can effectively suppress the unwanted qubit–coupler interactions to the residual coupling strength below 20 kHz. On the other hand, the effective coupling strength between adjacent qubits is approximately 3.5 MHz within one unit and 4.5 MHz between neighboring units, as indicated in Fig. S6F.

In our design, we carefully optimized the frequencies of adjacent coupler buses to maintain a frequency detuning exceeding 1 GHz, thereby effectively mitigating unwanted interaction between the next-nearest-neighbor (NNN) qubits through the virtual exchange interaction, which, in our setup, is very small (~ 0.08 MHz) and can therefore be considered negligible. The magnified micrographs in the insets of Fig. S3B illustrate the following regions: the coupling capacitor between the transmon qubit and the readout resonator, the capacitor between the transmission line and the band-pass filter, and the Manhattan-style superconducting Josephson junction (*57*).

As illustrated in Fig. S3C, the control-line coupler of each qubit is patterned on the backside of the chip with a minimalistic design, consisting solely of an arc-shaped gap around the pin–chip contact point (green). In Fig. S3E, the schematic of the qubit and control circuits is presented, illustrating how the microwave-frequency drive signals and low-frequency bias signals couple to the qubit. When a DC signal is applied to the control pin, the current is asymmetrically distributed around the gap, generating a differential magnetic flux $\Phi = \Phi_1 - \Phi_2$ within the superconducting qubit loop, where Φ_1 and Φ_2 denote the respective magnetic fluxes penetrating through the two half SQUID loops. This differential magnetic flux Φ_{ext} is the effective magnetic flux bias for the tunable transmon qubit. The dependence of the qubit frequency on Φ_{ext} can be approximated by (*28*):

$$\omega(\Phi_{\mathrm{ext}}) = \left(\omega_{\max} + \frac{E_{\mathrm{C}}}{\hbar}\right)\sqrt{d^2 + (1-d^2)\cos^2\left(\frac{\pi\Phi_{\mathrm{ext}}}{\Phi_0}\right)} - \frac{E_{\mathrm{C}}}{\hbar}. \tag{S4}$$

Here, E_{C} is the transmon charging energy, and $\omega_{\max} = (\sqrt{8E_{\mathrm{J}}E_{\mathrm{C}}} - E_{\mathrm{C}})/\hbar$ represents the maximum qubit frequency. The asymmetry parameter d of the SQUID junctions is defined as $d = |(E_{\mathrm{J},2} - E_{\mathrm{J},1})/(E_{\mathrm{J},2} + E_{\mathrm{J},1})|$, where $E_{\mathrm{J},1}$ and $E_{\mathrm{J},2}$ denote the Josephson energies of the two SQUID junctions. It is important to note that Eq. (S4) is an approximation, valid only in the

regime where $E_{\mathrm{J}} \gg E_{\mathrm{C}}$. When a high-frequency drive signal is applied, the electromagnetic field couples to the qubit via the effective mutual capacitance. In our chip, the control port exhibits mutual inductive (Z) coupling of approximately 0.8 pH. The capacitive (XY) coupling to the qubit is represented in the qubit decay rate of $2\pi \times 200$ Hz to the port. The inductive and capacitive coupling strengths can be independently modulated through modifications to the angle and size of the gap in the backside ground plane.

S3 Fabrication

Our sample is fabricated on a 3-inch silicon wafer with (100) crystal orientation and a resistivity of more than $20\,\mathrm{k}\Omega \cdot \mathrm{cm}$. The fabrication process is outlined as follows:

1. **Through-silicon vias (TSVs) fabrication**: Etch the vias using the deep reactive ion etching technique.

2. **TiN-film deposition**: Deposit 100-nm-thick TiN films on both sides of the silicon wafer with sputtering at a temperature of 850°C immediately after the wafer pre-cleaning.

3. **Via metallization**: Evaporate 300-nm-thick aluminum with an incident angle of 40° on both the front and back sides of the wafer on a planetary rotating stage.

4. **Aluminum-film etching**: Laminate resist films on both sides of the wafer and perform UV exposure and development, leaving the resist covering the vias. Perform wet etching to remove the aluminum on both sides of the wafer.

5. **TiN-film etching**: Spin-coat the wafer with AZ1500 photoresist, Then, do the photolithography using direct laser writing on each side of the wafer sequentially to define the qubits and resonators on the top surface and control-line contacts on the backside. Subsequently, perform dry etching on both sides after development.

6. **Cleaning**: Immerse the wafer in Remover104 at 120°C for more than four hours, then perform the oxygen plasma cleaning and HF cleaning.

7. **Junction fabrication**: Spin-coat the wafer with Copolymer and PMMA sequentially to form a bilayer electron-beam resist structure. Then, expose the wafer in an electron-beam writer. After developing the resist, evaporate aluminum films for the junctions (Fig. S3B) in an e-gun evaporator.

8. **Indium evaporation**: Cover the backside of the wafer with lamination film resist. Then, expose the wafer by a direct laser writer. After the development, evaporate 4-μm-thick indium on the backside of the chip.

9. **Dicing and lift-off**: Dice the wafer into chips and finally perform the lift-off.

S4 Device parameters

Our superconducting quantum processor employs frequency-tunable transmon qubits with a gradiometric structure, which enhances resilience against uniform global flux noise. The maximum frequencies of the qubits alternate between high and low values, as depicted in Fig. S5B. This frequency arrangement effectively reduces the interactions among the adjacent qubits when we characterize them at the beginning without bias currents (all the qubits will be at their sweet points if there are no flux offsets). In the experiments (see Fig. S9), we use DC currents to bias all the qubits at the same operation frequency while preparing their initial states and performing their readout at their individual idle frequencies with additional Z-pulses applied. As demonstrated in Fig. S6E, by ensuring sufficient frequency detuning between all the neighboring qubits, we suppress the ZZ coupling (*58*) to be below 110 kHz. This allows the fidelities of simultaneous single-qubit gates to be comparable to those of individual single-qubit gates. Moreover, the single-qubit gates are characterized by randomized benchmarking (*59–61*) at the idle frequencies with the Z-pulses applied. The achieved fidelities of the single-qubit gates suggest that both the Z-pulse distortion and crosstalk are well calibrated (see for the details in Sections S5.1 and S5.3.)

In our chip, the qubit anharmonicity η (representing the nonlinear boson–boson interaction on site) ranges from -248 to -218 MHz, which is more than 40 times larger than the coupling strength

Table S1: **Qubit parameters**. For better comparison, we show the simultaneous-readout assignment fidelity F_{ii} (the probability of correctly classifying the qubit state $|i\rangle$ as i), qubit idle-point thermal population $P_{\rm th}^{\rm idle}$, qubit operation-point thermal population $P_{\rm th}^{\rm op}$ measured when all the qubits are aligned at the operation frequency, and the fidelities of individual $P_{\rm RB}^{\rm ind}$ and simultaneous $P_{\rm RB}^{\rm sim}$ single-qubit gates, performed at the idle points with the Z-pulses applied. RB stands for randomized benchmarking.

Parameters	Q_0	Q_1	Q_2	Q_3	Q_4	Q_5	Q_6	Q_7
$F_{00}(\%)$	99.74	99.42	99.82	99.74	99.79	99.56	99.74	99.72
$F_{11}(\%)$	98.75	98.82	98.85	98.24	99.05	98.43	98.61	97.09
$P_{\rm th}^{\rm idle}(\%)$	1.39	1.9	2.58	0.75	0.46	3.81	5.39	2.46
$P_{\rm th}^{\rm op}(\%)$	4.62	4.26	4.22	5.09	5.09	5.21	5.16	5.24
$P_{\rm RB}^{\rm ind}(\%)$	99.25	99.44	99.48	99.66	99.54	99.52	99.05	99.44
$P_{\rm RB}^{\rm sim}(\%)$	99.39	98.44	99.60	99.29	99.68	99.31	98.92	99.66
Parameters	Q_8	Q_9	Q_{10}	Q_{11}	Q_{12}	Q_{13}	Q_{14}	Q_{15}
$F_{00}(\%)$	99.08	99.05	99.90	99.49	99.61	99.87	99.07	99.62
$F_{11}(\%)$	96.68	98.87	96.67	97.82	98.85	98.57	97.55	97.20
$P_{\rm th}^{\rm idle}(\%)$	2.85	2.6	1.22	0.56	4.04	4.12	4.13	2.63
$P_{\rm th}^{\rm op}(\%)$	5.14	5.04	4.88	5.24	4.78	3.94	4.43	4.93
$P_{\rm RB}^{\rm ind}(\%)$	97.91	99.44	99.44	99.58	99.81	99.43	99.63	99.61
$P_{\rm RB}^{\rm sim}(\%)$	97.14	99.47	98.84	99.64	98.92	99.18	99.25	99.63

between the neighboring qubits. Consequently, our system is in the hard-core limit of the interacting boson model and well described by the XY model (*32*). For the qubit-state readout, we use a resonator dispersively coupled to the transmon qubit to perform non-destructive measurement (*28*). A band-pass filter (*51, 62*) is used to indirectly couple the readout resonators to the transmission line (as illustrated in Fig. S3), achieving an average qubit–resonator coupling strength of approximately $2\pi\times150$ MHz (see Fig. S6B), while maintaining the Purcell-limited relaxation times for all the qubits longer than 1 ms. This results in a relatively large ratio between the dispersive shift χ and the readout-resonator decay rate κ with the median value of $|2\chi/\kappa|$ being 0.7 across all the qubits, allowing us to attain a high signal-to-noise ratio (SNR) for the readout (*63*).

As illustrated in Fig. S7, the single-qubit gates and readout are performed at the idle points

with the Z-pulses applied. During the waiting time of 600 μs, the Z-pulses are turned off. Then all the qubits are aligned to the operation point. With well-suppressed Z-pulse distortion and crosstalk, high-fidelity simultaneous single-qubit gates, and low readout crosstalk, we achieved an average simultaneous-readout assignment fidelity of 99.6% for state $|0\rangle$ and 97.5% for state $|1\rangle$ across all the qubits. Due to the extended waiting time at the operation point between two successive measurements, similar thermal populations $P_{\text{th}}^{\text{op}}$ were observed among all the qubits. Here, the thermal population of each qubit was estimated from the single-shot readout result from the first measurement M_0 and the second measurement M_1, given by $P_{\text{th}} = F_{00}^{0} - F_{00}^{1}$, where F_{00}^{1} is determined by post-selecting data from the second measurement M_1 in which the qubit was in state $|0\rangle$ in the first measurement M_0. In addition, we measured the thermal population of each qubit biased at the idle point by a DC current. The measured thermal populations $P_{\text{th}}^{\text{idle}}$ at the idle points are summarized in Table S1. From these thermal-population values, the effective qubit temperature was calculated (*64*) and shown in Fig. S6C. More parameters of the chip can be found in Table S1 and Figs. S5 and S6.

S5 System calibration

In the experiments, all the qubits are initially biased at the operation frequency with the Z-control DC bias (Z-bias), while the initial-state preparation and the final-state readout are performed at the idle points by applying Z-pulses. To achieve optimal energy-relaxation times T_1 across all qubits, minimize the impact of defects and ZZ coupling, and achieve high-fidelity multi-qubit initialization and readout, the following parameters need to be carefully optimized or calibrated: (i) Z-pulse distortion, (ii) qubit frequency setup, (iii) single-qubit gates, (iv) timing alignment between different control channels, (v) qubit frequency alignment, (vi) the phase of qubit, and (vii) qubit frequency over time . The qubit-frequency drift is evaluated with the Ramsey decay measurement and then corrected with the compensating Z-bias. For timing alignment and single-qubit gate optimization, we follow the methods in Ref. (*32*). Further details regarding the optimization and calibration of other parameters are provided below.

S5.1 Z-pulse distortion calibration

In our experiments, the Z-pulse distortion would significantly affect the fidelities of gates and readout since they are performed at the idle points with Z-pulses applied. Any component with limited bandwidth, impedance mismatch, or parasitic capacitance and inductance in the control line can contribute to the Z-pulse distortion. As shown in Fig. S3A, we use spring contacts to deliver the control signals to the ports on the chip. By employing the impedance-matched design, we can effectively suppress the distortion of the Z-pulse on the package side.

To calibrate the Z-pulse distortion, we need to bias each qubit to a point where its frequency is highly sensitive to the Z-pulse amplitude. In our case, the qubit is biased below 5.8 GHz, with the Z-pulse amplitude significantly larger than that used in the experiments. Since the tunable transmon qubit exhibits shorter T_2 at the frequency-sensitive point, the standard Ramsay pulse sequence to measure the phase shift due to the Z-pulse Fig. S8B (*65*) cannot be used for long-time-scale distortion due to the large dephasing rate. Therefore, we first calibrate the distortion of the Z-pulse using the waveform sequence shown in Fig. S8A (*32*) by applying a long-time (10 μs) Z-pulse. After a delay time τ, we apply two half-π pulses with a constant time spacing (200 ns) to measure the accumulated phase. The longtime Z-pulse can effectively separate the distortion due to the rising edge from that due to the falling edge, simplifying the calibration process. Then, we further characterize the short-time-scale Z-pulse distortions with the waveform sequence in Fig. S8B, as the accumulated phase measured in this waveform is more sensitive to the initial portion of the distorted Z-pulse. Finally, we find that applying several exponential-decay corrections to the ideal Z-pulse is sufficient to correct the distortion of the Z-pulse for all the qubits. In Fig. S8C, we present the accumulated phase of qubit Q_5 measured by using the sequence in Fig. S8A with corrected and uncorrected Z-pulses, respectively.

S5.2 Frequency setup

Several considerations must be taken into account when optimizing the frequency setup, as outlined below:

1. **Energy relaxation**: Due to unwanted coupling with two-level systems (TLSs) or other modes, the transmon qubits typically exhibit T_1 fluctuations as a function of the qubit frequency and time (*66, 67*). Consequently, we measure the T_1 distribution for each qubit in the frequency range between the operation frequency and the idle frequency, ensuring that none of the qubits interact with the loss modes.

2. **Qubit–qubit coupling at the idle points**: In our chip, the coupling strengths between nearest-neighbor (NN) qubits range from 2.9 to 4.8 MHz. After optimizing the idle frequencies of all the qubits, the residual XY coupling between all the NN qubits can be suppressed below 0.06 MHz. Additionally, we ensure that the minimum frequency detuning between the next-nearest-neighbor (NNN) qubits is larger than 5 MHz to suppress any unwanted qubit drive from the X-crosstalk, which should be below -30 dB in our system. Finally, to avoid the potential two-photon excitations due to the X-crosstalk, we also avoid exact frequency matches with $\omega_{02}/2$ between the neighboring qubits, where ω_{02} is the frequency difference between the ground state and the second excited state.

3. $\boldsymbol{ZZ}$ **coupling**: For coupled two neighboring transmon qubits, because of the weak anharmonicities, there is non-negligible ZZ coupling due to interaction through higher-energy levels such as $|11\rangle, |02\rangle$, and $|20\rangle$ (*58*). This coupling can be expressed as

$$\Omega_{ZZ} = -\frac{2g^2(\eta_1 + \eta_2)}{(\Delta - \eta_1)(\Delta + \eta_2)}, \tag{S5}$$

where η_1 and η_2 represent the anharmonicity of the qubits, g is the their coupling strength, and Δ denotes the difference in their frequencies. The ZZ interaction introduces inter-qubit control crosstalk during parallel quantum operations, thereby reducing the fidelity of multi-qubit state initialization. Furthermore, this parasitic coupling degrades the fidelity of simultaneous readout for the multi-qubit state. Consequently, the final state of the quantum system continues to evolve under the non-negligible ZZ coupling. By optimizing the fre-

quency setup, as shown in Fig. S6G, we suppressed the ZZ coupling between any NN qubits to below 110 KHz.

4. **Dephasing**: In our chip, T_1 is always much larger (>10 μs) than the system evolution time for the experiment (300 ns). However, the short dephasing time (as shown in Fig. S5) could significantly influence the experiment. The qubits may couple to some modes with thermal population (TLSs, etc.), resulting in a significantly larger dephasing rate, which can lead to reduced purity in the multi-qubit states. By measuring $T_2^\star$ of each qubit within a frequency range of several tens of MHz, both at the operation point and the idle points, we might find the undesired coupling modes. To avoid these modes, we adjust the operation point or the idle points of the affected qubits, ensuring that they are decoupled from these modes. After this optimization, all the qubits work well at the operation point and their idle points.

S5.3 Qubit-frequency alignment

In Ref. (*32*), the frequency alignment was optimized by the vacuum Rabi oscillations between the nearest-neighbor qubits. Then, the Z-pulses, corrected by the crosstalk matrix, were applied to shift the qubits from the idle points to the operation point. However, in this experiment, we employed an alternative approach to align the frequencies of all the qubits, omitting the Z-pulse correction by the crosstalk matrix, as the current chip exhibits Z-crosstalk nearly ten times smaller. The details of the calibration process are as follows:

1. Bias each qubit to the operation point using Z-bias, while detuning the frequencies of other qubits by more than 400 MHz. Next, perform the Ramsey measurement to fine-tune the Z-bias voltage $V_{\rm DC}$, adjusting each qubit to the operation frequency.

2. Use the Z-pulse to shift each qubit from the operation point calibrated in step 1 to its idle point. Then, perform the Ramsey measurement at the idle point. Fine-tune the Z-pulse amplitude $V_{\rm pulse}$, setting each qubit to its target idle frequency.

3. Bias all the qubits at the operation point by Z-bias with the calibrated Z-bias voltage $V_{\rm DC}$

in step 1. Next, perform the Ramsey measurement for each qubit at its idle point with the calibrated Z-pulse amplitude V_{pulse} in step 2. If any qubits experience frequency shifts due to the Z-bias crosstalk, then, fine-tune the Z-bias voltage for those qubits to compensate for the frequency shifts, successfully calibrating the Z-bias crosstalk.

4. After calibrating each qubit's Z-bias voltage V_{DC} in step 3, we perform the Ramsey measurement on each qubit with all the qubits' Z-pulses applied. Due to Z-pulse crosstalk, some qubits may exhibit frequency shifts at their idle points. We then fine-tune the Z-pulse amplitudes of these qubits to compensate for the frequency shifts, successfully calibrating the Z-pulse crosstalk.

In the process of the Z-crosstalk calibration, we found that most qubits experienced frequency shifts of less than 1 MHz from the crosstalk of the Z-bias and the Z-pulse, signifying minimal Z-crosstalk within our system. As all calibrations above rely on the Ramsey-oscillation measurements, the frequency alignment precision is limited by the fitting error of the Ramsey oscillation, which is generally below 10 kHz. After calibration, we can mitigate the effects of the Z-crosstalk and ensure that each qubit functions at its target frequency during the experiments. As shown in Fig. S10, the experimental results for the 12Q chain system are in good agreement with the theoretical simulations.

S5.4 Relative-phase calibration

In the information leakage benchmark experiment, as illustrated in Fig. 4A of the main text, all qubits in the 3×3 array are initially prepared in a superposition state. Specifically, the center and corner qubits are prepared in the state $|X_+\rangle = \frac{1}{\sqrt{2}}(|0\rangle + |1\rangle)$, while the remaining qubits are prepared in the state $|Y_+\rangle = \frac{1}{\sqrt{2}}(|0\rangle + i|1\rangle)$. To prepare this multi-qubit state, we must calibrate the relative phases between all the qubits (*68*). The Hamiltonian for the coupled two-qubit system can be written as

$$\hat{H}/\hbar = \frac{1}{2}\omega\hat{\sigma}_z^i + \frac{1}{2}\omega\hat{\sigma}_z^j + g\left(\hat{\sigma}_+^i\hat{\sigma}_-^j + \hat{\sigma}_-^i\hat{\sigma}_+^j\right). \tag{S6}$$

Here, we assume that the two qubits have the same frequency ω, and g is the coupling strength between them. As shown in Fig. S11, in the relative-phase calibration of the two qubits, we use the initial phase of Q_i as a reference, preparing it to the state $|\psi_i\rangle = \frac{1}{\sqrt{2}}(|0\rangle + |1\rangle)$, then we prepare another qubit to the state $|\psi_j\rangle = (|0\rangle + e^{i\phi}|1\rangle)$ with relative phase ϕ. The initial state for the two-qubit system can be written as $|\psi_{ij}(t=0)\rangle = \frac{1}{2}(|0\rangle + |1\rangle) \otimes (|0\rangle + e^{i\phi}|1\rangle)$. Under Eq. (S6), we obtain the state evolution over time as follows:

$$\begin{aligned}
|\psi_{ij}(t)\rangle =& \frac{1}{2}e^{-i\omega t}|00\rangle + \frac{1}{2\sqrt{2}}e^{i\phi}(|\Psi_+(t)\rangle - |\Psi_-(t)\rangle) + \frac{1}{2\sqrt{2}}(|\Psi_+(t)\rangle + |\Psi_-(t)\rangle) + \frac{1}{2}e^{i\omega t}|11\rangle \\
=& \frac{1}{2}e^{-i\omega t}|00\rangle + \frac{1}{4}\left[(e^{-igt} - e^{igt}) + e^{i\phi}(e^{-igt} + e^{igt})\right]|01\rangle \\
&+ \frac{1}{4}\left[(e^{-igt} + e^{igt}) + e^{i\phi}(e^{-igt} - e^{igt})\right]|10\rangle + \frac{1}{2}e^{i\omega t}|11\rangle.
\end{aligned} \tag{S7}$$

Here, $|\Psi_+\rangle = \frac{1}{\sqrt{2}}(|01\rangle + |10\rangle)$ and $|\Psi_-\rangle = \frac{1}{\sqrt{2}}(|01\rangle - |10\rangle)$ are the eigenstates of the coupled qubits in Eq. (S6). Then, the probabilities for observing the four energy eigenstates $|00\rangle$, $|11\rangle$, $|01\rangle$ and $|10\rangle$ evolve as follows:

$$P_{00}(t) = \frac{1}{4}, \tag{S8}$$

$$P_{11}(t) = \frac{1}{4}, \tag{S9}$$

$$\begin{aligned}
P_{01}(t) &= \left|\frac{1}{4}\left[(e^{-igt} - e^{igt}) + e^{i\phi}(e^{-igt} + e^{igt})\right]\right| \\
&= \frac{1}{4}\left[1 - \sin(\phi)\sin(2gt)\right],
\end{aligned} \tag{S10}$$

$$\begin{aligned}
P_{10}(t) &= \left|\frac{1}{4}\left[(e^{-igt} + e^{igt}) + e^{i\phi}(e^{-igt} - e^{igt})\right]\right| \\
&= \frac{1}{4}\left[1 + \sin(\phi)\sin(2gt)\right].
\end{aligned} \tag{S11}$$

From Eqs. (S8)–(S11), we expect that the probabilities for states $|00\rangle$ and $|11\rangle$ are independent of the phase and time, each remaining constant at $1/4$. This is consistent with the experimental results presented in Fig. S12B. When the phase is neither 0 nor π, the probabilities P_{01} and P_{10} will oscillate with the phase ϕ of Q_j, ranging from $\frac{1}{4}[1 - \sin(2gt)]$ to $\frac{1}{4}[1 + \sin(2gt)]$. In the

relative-phase calibration, we fixed the evolution time to be $\pi/4g$ for better SNR. The position of the black arrow in Fig. S12B marks the phase offset between Q_3 and Q_7, where $P_{01} = 0$ with a negative slope. We calibrated the necessary qubit pairs to determine the relative-phase offsets between all the qubits in the 3 × 3 array. The results are presented in Fig. S12A.

S5.5 Dynamical-phase calibration

In the information-leakage benchmark experiment, we measured the expectation value $\langle X \rangle$ of all the qubits (Fig. 4A) with a $X_{\frac{\pi}{2}}$ pulse applied to each qubit before the measurement. As the system evolves with all the qubits at the operation point while being characterized at their idle points, all the qubits will accumulate a phase during the system evolution. We use the sequence in Fig. S13 to calibrate each qubit's dynamical phase. The qubit is prepared in the state $\frac{1}{\sqrt{2}}(|0\rangle + |1\rangle)$ at the idle point with the Z-pulse applied. Then, the Z-pulse is turned off, tuning the qubit to the operation point. After a time τ, the qubit is returned to the idle point, followed by an X rotation, and finally measured. The probability of measuring the qubit at state $|1\rangle$ oscillates when we sweep the phase of the final X rotation, allowing us to determine the accumulated dynamical phase at which the qubit reaches maximum probability at state $|1\rangle$. Specifically, the qubit accumulates its phase in three stages during the system evolution: the falling edge ($0 < t < \tau_\mathrm{f}$), the flat section ($\tau_\mathrm{f} < t < \tau_\mathrm{r}$) and the rising edge ($\tau_\mathrm{f} < t < \tau$):

$$\phi(\tau) = \int_0^{\tau_\mathrm{f}} \Delta\omega_\mathrm{r}(t)\, dt + \int_{\tau_\mathrm{f}}^{\tau_\mathrm{r}} \Delta\omega_\mathrm{r}(t)\, dt + \int_{\tau_\mathrm{r}}^{\tau} \Delta\omega_\mathrm{r}(t)\, dt. \tag{S12}$$

Finally, we sweep the evolution time τ, performing the $X_{\frac{\pi}{2}}$ rotation to the final state with the calibrated phase. As shown in Fig. S13B, the phases of all qubits' final states for each evolution time τ are well calibrated, and the decay rate of the qubit expectation values $\langle X \rangle$ agrees well with the qubit dephasing time T_2^* illustrated in Fig. S5H.

S5.6 Long-time readout stability

In our chip, four readout resonators in a single unit are coupled to a single band-pass filter. By applying frequency-multiplexed heterodyne-mixing signals to the filter, we realize multiplexed

qubit readouts through the four resonators. In the readout optimization, we fine-tune the readout frequencies, durations, and amplitudes to maximize the separation between the readout signals conditioned on the qubits' ground and excited states in the IQ plane. The hyperplane parameters are calculated to maximize the probability of correctly classifying the states $|0\rangle$ and $|1\rangle$. The readout quality is quantified by the readout fidelity, defined as

$$F_{\mathrm{RO}} = \frac{1}{2}(F_{00} + F_{11}), \tag{S13}$$

where F_{00} (F_{11}) is the probability of correctly classifying the qubit state $|0\rangle$ ($|1\rangle$) as 0 (1).

The readout pulse length for each readout resonator is approximately 400 ns, with a demodulation window duration ranging from 520 ns to 600 ns, primarily determined by the external coupling rate of each resonator, κ (as illustrated in Fig. S5H). Figure S14A illustrates a set of the single-shot readout data for Q_{12}. The data is acquired by preparing all qubits in the states $|0\rangle^{\otimes 16}$ (shown in blue) and $|1\rangle^{\otimes 16}$ (shown in red). The dashed line is the principal axis used to distinguish the qubit states $|0\rangle$ and $|1\rangle$. Figure S14B shows histograms of the data in Fig. S14A projected along the principal axis in the IQ plane. The dot-dashed lines represent the Gaussian fits to the signal distributions of states $|0\rangle$ and $|1\rangle$. For this dataset, the readout assignment fidelity is $F_{\mathrm{RO}} = 99.68\%$, with $F_{00} = 99.87\%$ and $F_{11} = 99.49\%$. The difference between F_{11} and F_{00} is attributed to the energy relaxation of the qubit during the readout.

In our experiments, we take the data continuously for a long time. To maintain the system stability, for every 3.5 hours, we calibrated each qubit's frequency and π-pulse amplitude and then characterized the readout fidelity without modifying any readout parameters. In Fig. S15, we present the results of readout data collected over five days of measurement. For most of the qubits, the readout remained highly stable, with variations in F_{ii} ($i \in \{0, 1\}$) below 0.02. Over five days of continuous measurement, we achieved an average readout fidelity F_{RO} of 98.51% across all the qubits, with average fidelities of 99.57% for F_{00} and 97.46% for F_{11}.

S6 Benchmark of many-body information leakage

In this section, we explore the universality of our method for benchmarking many-body information leakage. When the system is coupled to the environment, it transitions into a mixed state. The corresponding density matrix can be expressed as a sum of orthogonal pure states:

$$\hat{\rho} = \sum_j \lambda_j \left|\phi_j\right\rangle \left\langle\phi_j\right|, \tag{S14}$$

where $\langle\phi_i|\phi_j\rangle = \delta_{ij}$ and $\sum_j \lambda_j = 1$. Without loss of generality, we assume $\lambda_1 \geq \lambda_2 \geq \lambda_3 \ldots$. A large degree of information leakage results in low purity p of $\hat{\rho}$, defined as

$$p := \mathrm{Tr}\hat{\rho}^2 = \sum_j \lambda_j^2, \tag{S15}$$

and is related to the second-order Rényi entropy:

$$S_2 = -\ln \mathrm{Tr}\hat{\rho}^2 = -\ln p. \tag{S16}$$

We consider the case of small information leakage, where $\lambda_1 \gg \sum_{j=2} \lambda_j$. Under this condition, the second-order Rényi entropy can be approximated as

$$S_2 = -\ln\left(\sum_j \lambda_j^2\right) \sim -2\ln\lambda_1. \tag{S17}$$

Now we focus on the projected ensemble of the density matrix $\hat{\rho}$. Each projected state of subsystem A can be expressed as

$$\hat{\rho}_{\mathrm{A}}(z_{\mathrm{B}}) = \sum_j \lambda_j \left|\phi_{\mathrm{A},j}(z_{\mathrm{B}})\right\rangle \left\langle\phi_{\mathrm{A},j}(z_{\mathrm{B}})\right|, \tag{S18}$$

where $|\phi_{\mathrm{A},j}(z_{\mathrm{B}})\rangle$ represents the projected state corresponding to $|\phi_j\rangle$:

$$\left|\phi_{\mathrm{A},j}(z_{\mathrm{B}})\right\rangle = \mathcal{A}(\mathbb{I}_{\mathrm{A}} \otimes \left\langle z_{\mathrm{B}}\right|) \left|\phi_j\right\rangle, \tag{S19}$$

with $\mathcal{A}$ as the normalization factor. In a quantum many-body system, after sufficient time evolution, $|\phi_{\mathrm{A},j}(z_{\mathrm{B}})\rangle$ can be treated as a random state. Using the Bloch-sphere representation, $\hat{\rho}_{\mathrm{A}}(z_{\mathrm{B}})$ can be regarded as the sum of a series of random vectors. In the case of small information leakage, the

length of these vectors (equivalent to the purity) is proportional to λ_1. Consequently, the ensemble-averaged entropy of $\hat{\rho}$ can be approximated as

$$\bar{E}_{\mathrm{A}} = -\sum_{z_{\mathrm{B}}} p(z_{\mathrm{B}}) \ln \mathrm{Tr}\hat{\rho}_{\mathrm{A}}^2(z_{\mathrm{B}}) \sim -\ln \lambda_1. \tag{S20}$$

From Eqs. (S17) and (S20), we can find that $\bar{E}_{\mathrm{A}}$ is proportional to the second-order Rényi entropy S_2. This demonstrates that $\bar{E}_{\mathrm{A}}$ serves as an effective measure of information leakage in quantum many-body systems.

To validate the above discussions, we perform numerical simulations for both Markovian noise and $1/f$ noise. We consider three representative models: the 1D mixed Ising model, the effective Hamiltonian for Rydberg atoms with long-range van der Waals interaction, and the XY model. The corresponding Hamiltonians are written as:

$$\hat{H}_{\mathrm{MIsing}} = \sum_{j}^{L-1} \hat{\sigma}_j^z \hat{\sigma}_{j+1}^z + h_z \sum_{j=1}^{L} \hat{\sigma}_j^z + h_x \sum_{j=1}^{L} \left(\hat{\sigma}_j^x - \hat{\sigma}_1^z - \hat{\sigma}_L^z\right), \tag{S21}$$

$$\hat{H}_{\mathrm{RA}} = V \sum_{i>j}^{L-1} \frac{\hat{n}_j \hat{n}_{j+1}}{|i-j|^6} - \Delta \sum_{j=1}^{L} \hat{n}_j + \Omega \sum_{j=1}^{L} \hat{\sigma}_j^x, \tag{S22}$$

$$\hat{H}_{\mathrm{XY}} = \sum_{\langle i,j \rangle} J_{ij} (\hat{\sigma}_i^+ \hat{\sigma}_j^- + \mathrm{h.c.}). \tag{S23}$$

In addition, without loss of generality, we only consider the infinite-temperature systems.

S6.1 Markovian noise

We first consider Markovian noise, where the system dynamics are governed by the Lindblad master equation:

$$\frac{d}{dt}\hat{\rho} = -i[\hat{H}, \hat{\rho}] + \sum_j \gamma_j \left(\hat{L}_j \hat{\rho} \hat{L}_j^\dagger - \frac{1}{2}\{\hat{L}_j^\dagger \hat{L}_j, \hat{\rho}\}\right). \tag{S24}$$

Here, γ_j represents the dissipation rate (the coupling strength between the system and the environment), and $\hat{L}_j$ is the jump operator.

For 1D mixed Ising model, we choose the parameters $h_z = 0.8090$, $h_x = 0.9045$, and $L = 10$, and also consider the dephasing channel $\hat{L}_j = \hat{\sigma}_j^z$. In addition, we consider three initial states: $|\Psi_1\rangle = |Y_+ Y_+ Y_+ Y_+ ...\rangle$, $|\Psi_2\rangle = |Y_+ Y_- Y_+ Y_- ...\rangle$, and $|\Psi_3\rangle = |X_+ X_- X_+ X_- ...\rangle$.

For $\hat{H}_{\mathrm{RA}}$, we choose the parameters $V = 1.44$, $\Delta = 0.9$, $\Omega = 4.7$, and $L = 10$, and consider the energy-relaxation channel $\hat{L}_j = \hat{\sigma}_j^-$. We consider three initial states: $|\Psi_1\rangle = |Y_+Y_+Y_+Y_+...\rangle$, $|\Psi_2\rangle = |0000...\rangle$, and $|\Psi_3\rangle = |0101...\rangle$.

For the XY model, we consider both 1D and 2D systems with the dephasing channel $\hat{L}_j = \hat{\sigma}_j^z$, and the system sizes are $L = 10$ and 3×3, respectively. In the 1D case, we consider three initial states: $|\Psi_1\rangle = |X_+Y_+X_+Y_+...\rangle$, $|\Psi_2\rangle = |X_+X_+X_-X_-X_+X_+X_-X_-X_+X_+\rangle$, and $|\Psi_3\rangle = |X_+X_+Y_+Y_-X_+ X_+Y_+Y_-X_+X_+\rangle$. In the 2D case, we have $|\Psi_1\rangle = |X_+Y_+X_+Y_+...\rangle$, $|\Psi_2\rangle = |X_+X_+X_+X_-X_-X_-X_+X_+X_+\rangle$, and $|\Psi_3\rangle = |X_+X_-X_-Y_+Y_-Y_-X_+X_-X_-\rangle$.

The numerical results are presented in Fig. S16. The left panels demonstrate that $\bar{E}_{\mathrm{A}}$ exhibits similar dynamics across different subsystems A. In the short-time regime ($t \ll 1/\gamma$), both S_2 and $\bar{E}_{\mathrm{A}}$ show a linear increase. Over a longer time scale, the dynamics of $\bar{E}_{\mathrm{A}}$ can be well approximated by

$$\bar{E}_{\mathrm{A}} = E_0(1 - e^{-t/\tau_{\mathrm{MB}}}), \tag{S25}$$

where E_0 and τ_{MB} characterize the steady-state value and relaxation time, respectively. The middle panels reveal that $\bar{E}_{\mathrm{A}}$ is largely independent of the initial states. We also obtain the slopes of $S_2(t)$ and $\bar{E}_{\mathrm{A}}(t)$ in the short-time regime by using a linear fit. The slopes versus the dissipation rate γ are plotted in the right panels of Fig. S16. The results indicate that the slopes are proportional to γ.

S6.2 1/f noise

In many quantum simulators, dephasing mainly results from $1/f$ noise (e.g., superconducting qubits, nuclear spins, Rydberg atoms etc.), which is not Markovian. Now we focus on $1/f$ noise, where the system dynamics are governed by the Hamiltonian:

$$\hat{H}(t) = \hat{H}_0 + \frac{1}{2}\sum_j \xi_j(t)\hat{\sigma}_j^z, \tag{S26}$$

$$\langle \xi_j(0)\xi_k(t)\rangle = \int_{-\infty}^{\infty} \frac{d\omega}{2\pi} S_{jk}(\omega)e^{-i\omega t}. \tag{S27}$$

where $\xi(t)$ is a Gaussian fluctuation, and $S_{jk}(\omega)$ is the spectral density of the noise. Here, we do not consider the spatial correlation of the noise, so the noise spectral density of noise satisfies

$$S_{jk}(\omega) = \frac{\delta_{jk} A_j}{|\omega|}, \tag{S28}$$

where A_j is the noise strength. Generally, the low-frequency regime of $1/f$ noise dominates the dephasing in the system, i.e., $\omega_h \ll 1/T$, where ω_h is the high-frequency cutoff and T is the total evolution time. Thus, Eq. (S26) can be considered as a time-independent system with disorder.

S7 Other extended data

In the section, we present more experimental and numerical data (Figs. S18 – S21).

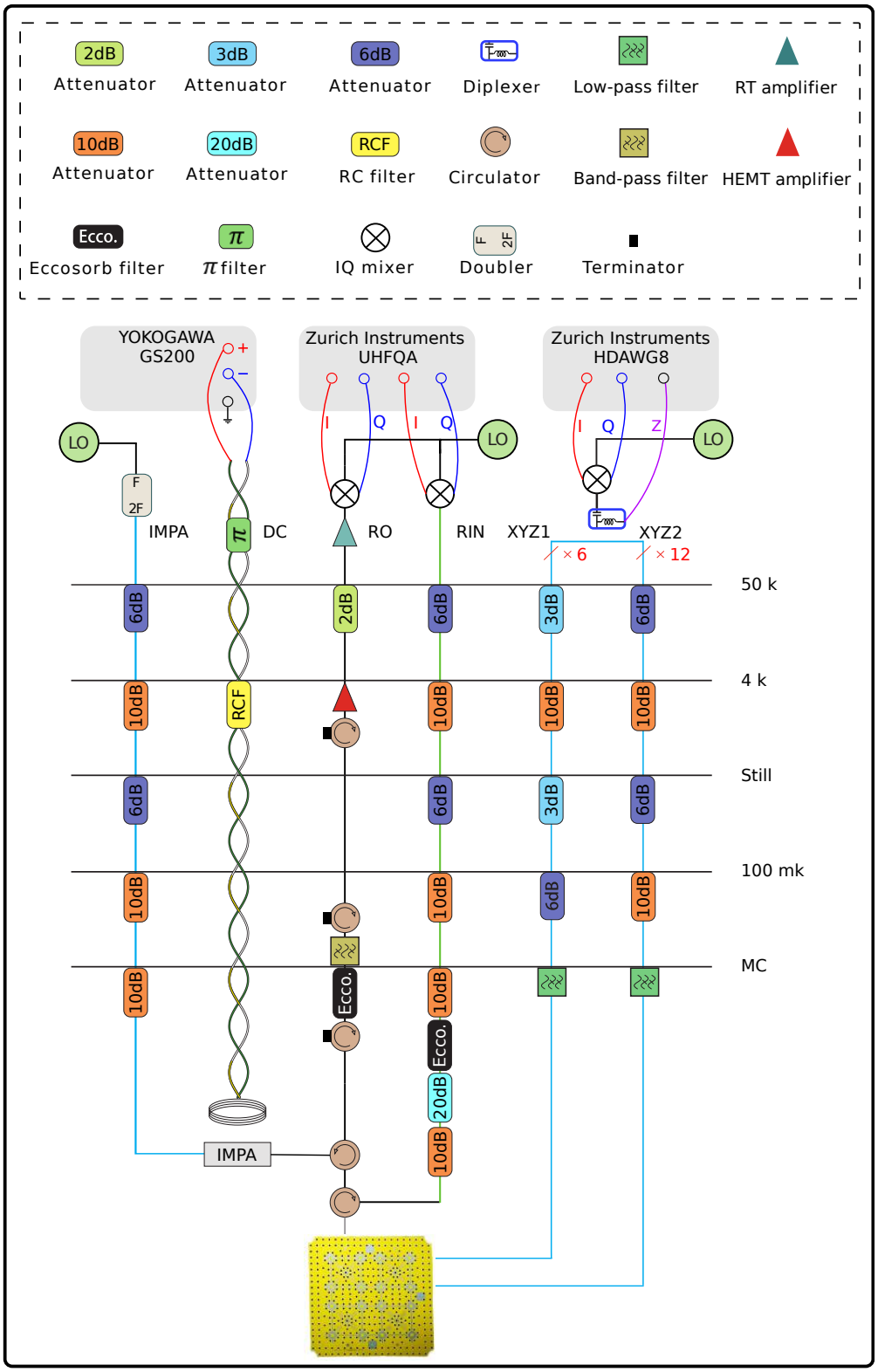

Figure S1: **Measurement setup**.

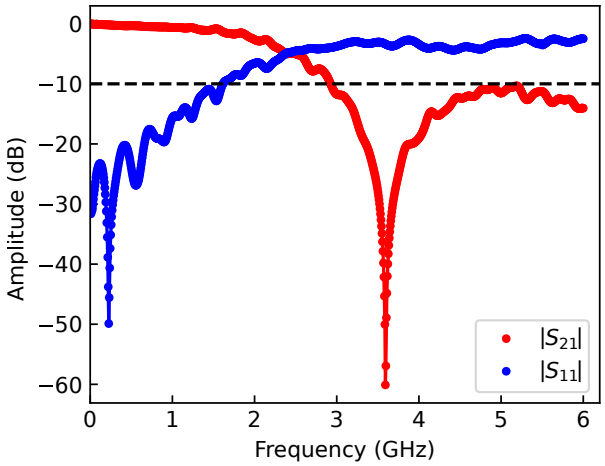

Figure S2: $|S_{11}|$ **and** $|S_{21}|$ **of the homemade low-pass filter.**

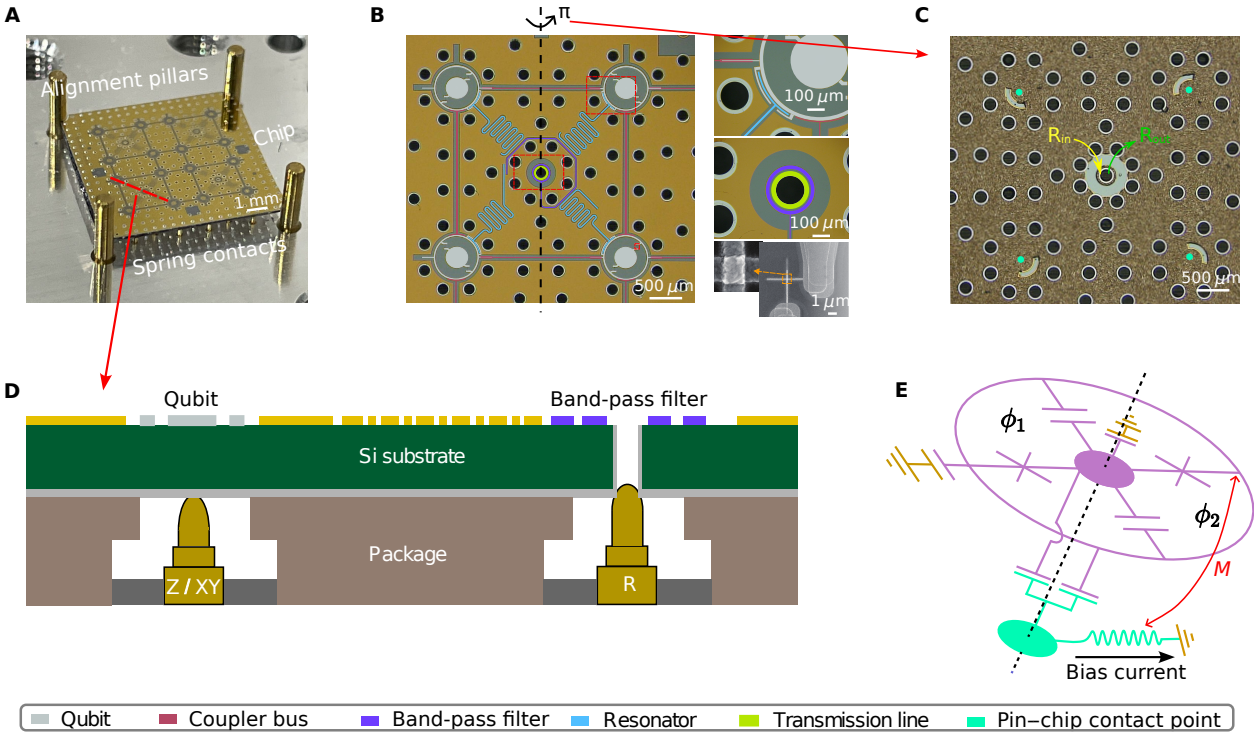

Figure S3: **Package and the chip.** **A**, Optical images of the assembly of the package and chip. **B**, False-colored image of the top side of the chip. The insets show the magnified images of the parts enclosed in the red squares. The Josephson junction area is approximately 180×210 nm^2. **C**, Backside of the chip. **D**, Schematic diagram of the cross-sectional profile along the dashed line in **A**. **E**, Schematic circuit diagram of the qubit and control circuits.

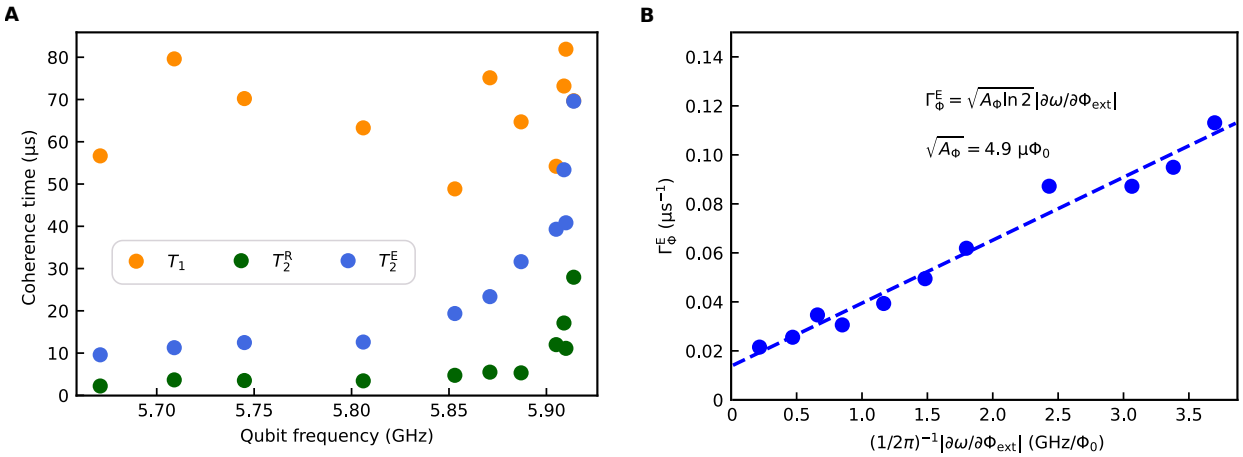

Figure S4: **Decoherence characterization.** **A**, Qubit coherence time T_1 (energy relaxtion), T_2^{R} (Ramsey), and T_2^{E} (spin-echo) as a function of the qubit frequencies. The data is for Q_{11}. **B**, Pure dephasing rates $\Gamma_\varphi^{\mathrm{E}}$ as a function of the slope of the qubit spectrum. We derive the $1/f$ flux-noise amplitude $\sqrt{A_\Phi}$ through the linear fit to the data.

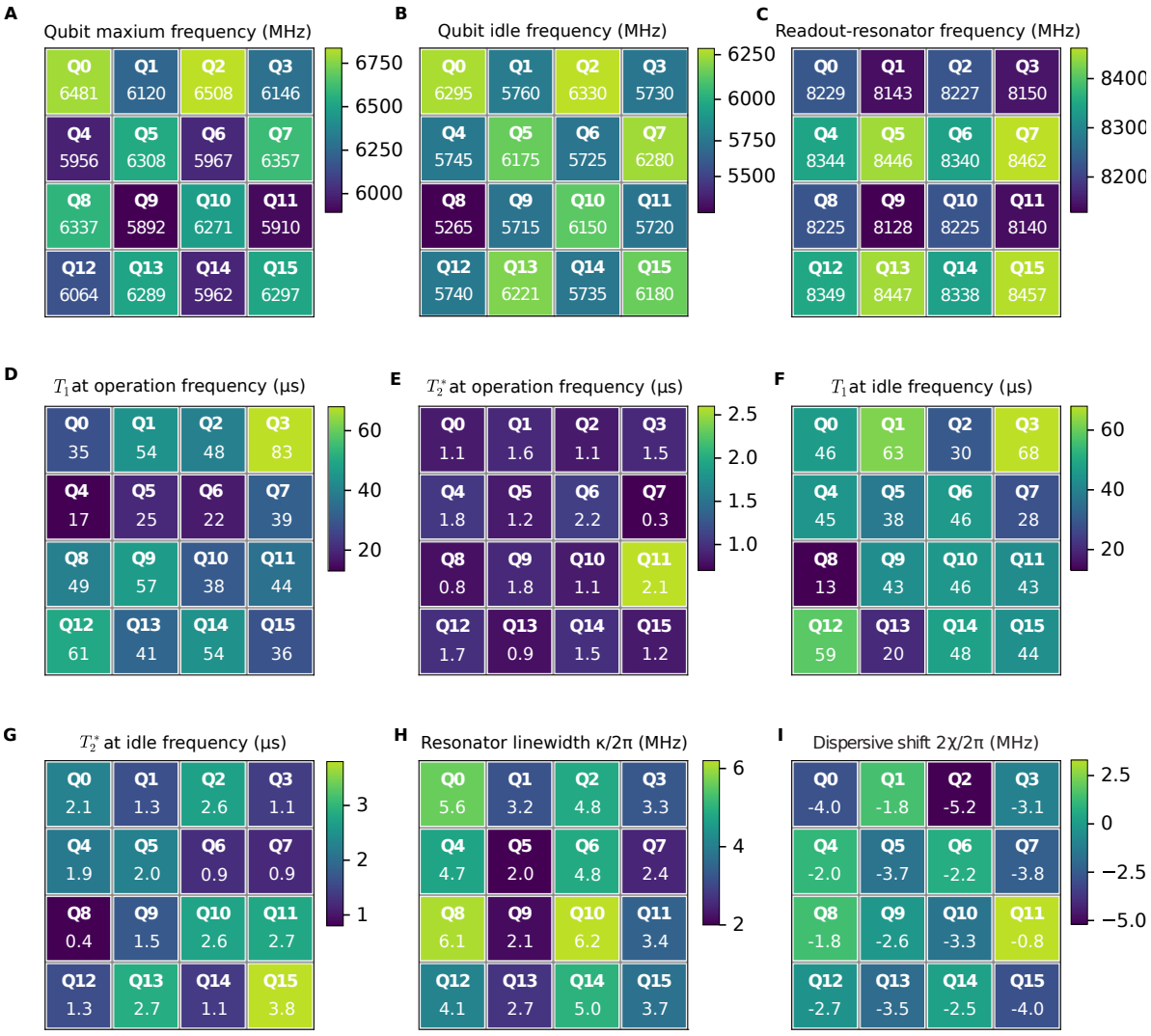

Figure S5: **Chip parameters**. **A**, Qubit maximum frequencies. **B**, Qubit idle frequencies. **C**, Readout-resonator frequencies. **D** and **E**, T_1 and T_2^* at the operation frequency. **F** and **G**, T_1 and T_2^* at the idle frequencies. **H**, Readout-resonator linewidths κ. **I**, Dispersive shifts of the readout resonators, 2χ.

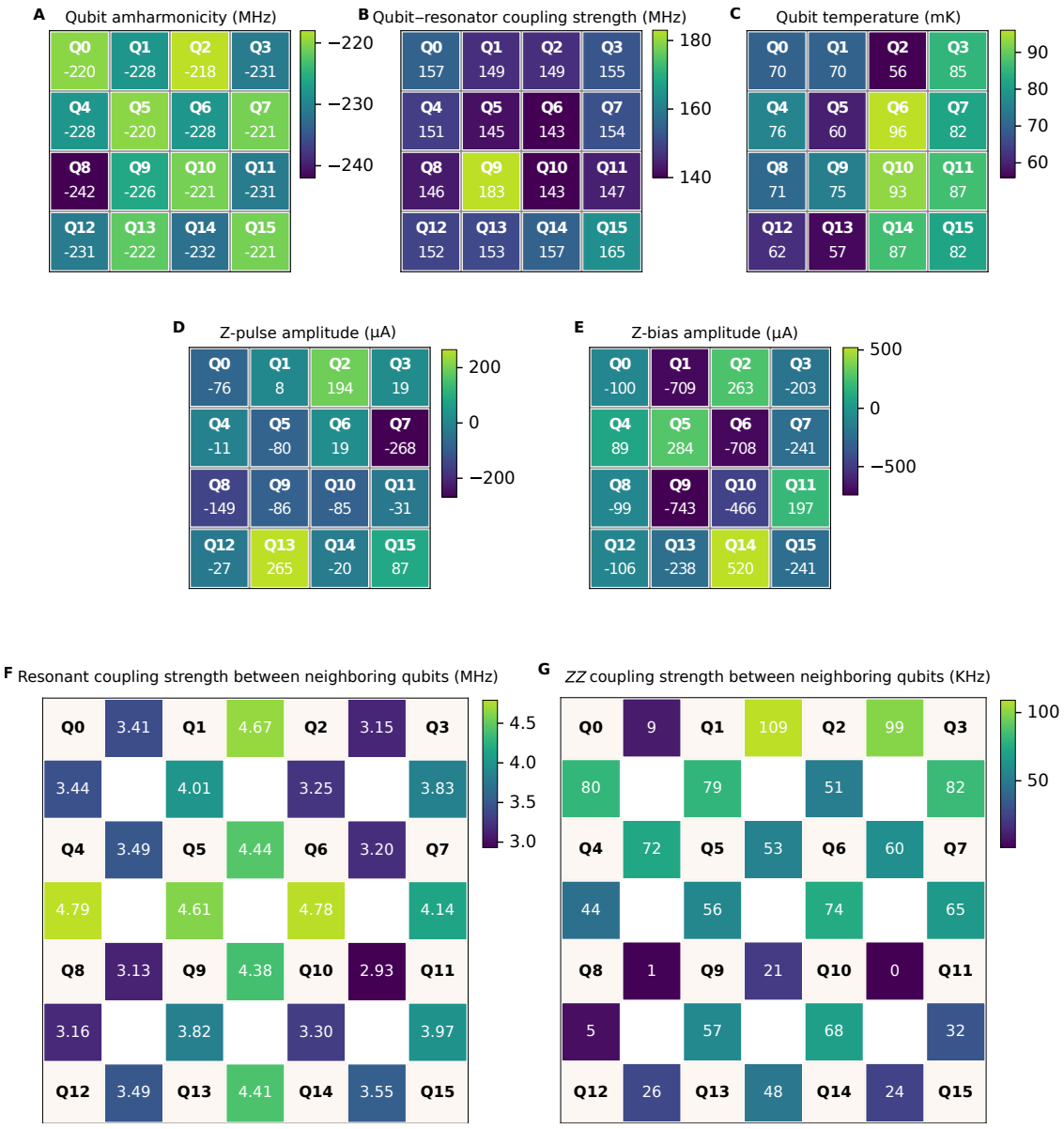

Figure S6: **Chip parameters**. **A**, Qubit anharmonicity η. **B**, Qubit–resonator coupling strength. **C**, Effective qubit temperature at the idle point. **D**, Z-pulse amplitude used to bias the qubit from the working point to the idle point. **E**, Z-bias amplitude used to bias the qubit at the operation point. **F**, Coupling strength between the neighboring qubits. **G**, ZZ-coupling strength between the neighboring qubits.

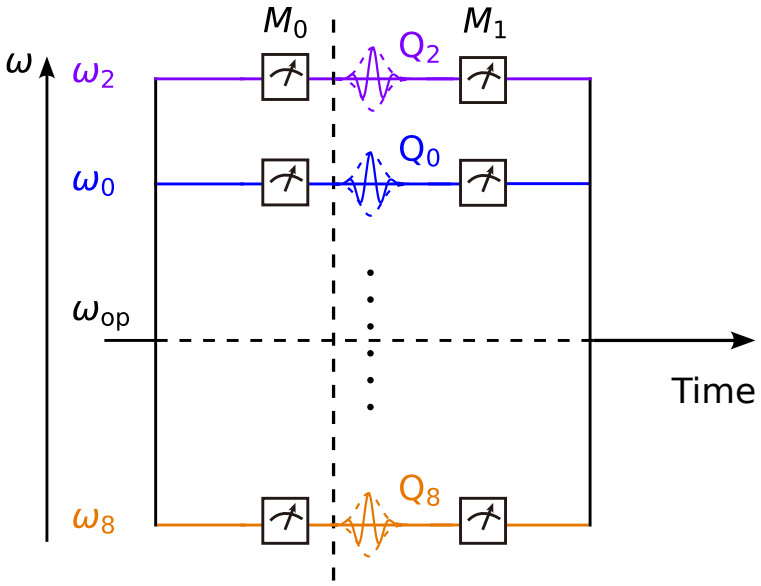

Figure S7: **Pulse sequence for evaluating assignment fidelities:** All the qubits are Z-biased at the operation frequency ω_{op} for initialization for a long period (600 μs) to allow the system to reach a steady state. Then, we apply the Z-pulses to shift all the qubits to their idle frequencies. Subsequently, we perform the first measurement M_0, apply qubit drives, and conduct the second measurement M_1, sequentially.

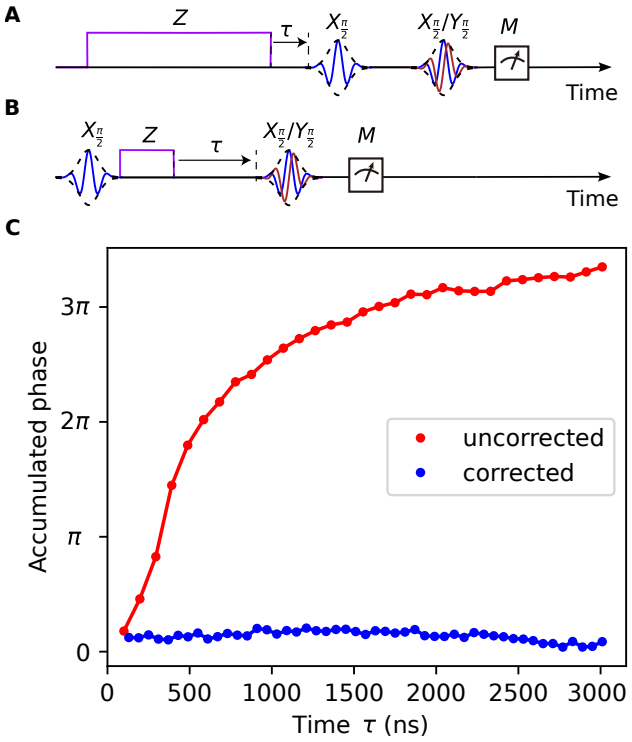

Figure S8: ***Z*-pulse distortion calibration**. **A**, Pulse sequence to calibrate the long-time-scale Z-pulse distortion. **B**, Pulse sequence to calibrate the short-time-scale Z-pulse distortion. **C**, Accumulated phase measured by the pulse sequence in **A** before and after the Z-pulse distortion calibration.

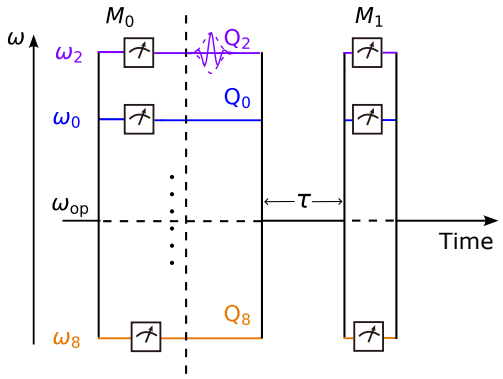

Figure S9: **Pulse sequence to probe deep thermalization**. All the qubits are initially aligned to the operation point. Then, we turn on the Z-pulses, perform the readout M_0 and prepare the initial state. Subsequently, we turn off the Z-pulses, allowing the system to evolve at the operation point for a duration of τ. Finally, the Z-pulses for all the qubits are turned on to freeze the system evolution and perform the readout M_1.

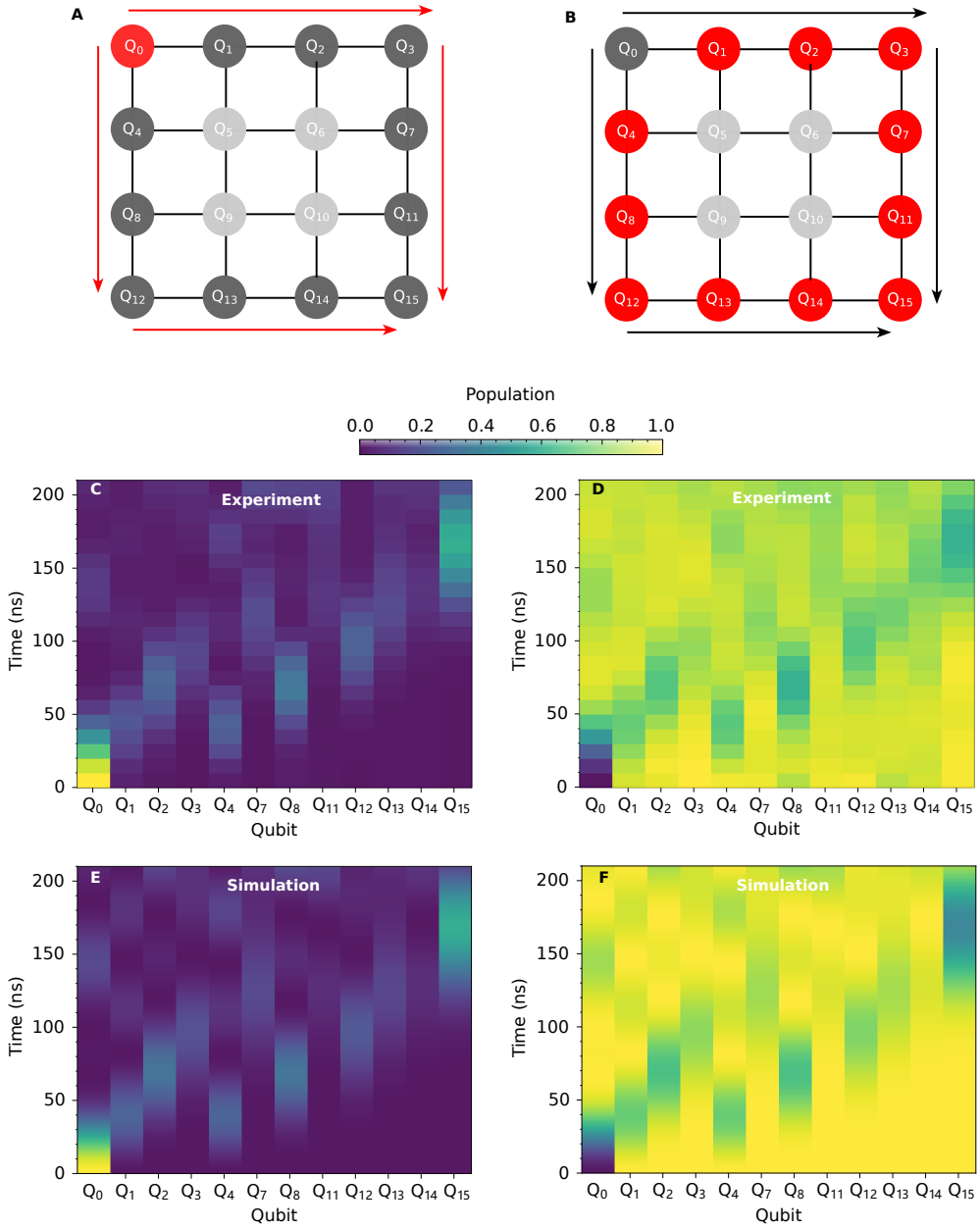

Figure S10: **Dynamics of particle and hole propagating along a 12-qubit loop**. **A**, Q_0 is initially excited to the state $|1\rangle$ while all other qubits are in state $|0\rangle$, creating a localized particle which propagates along the 12-qubit loop. **B**, All the qubits except Q_0 are initially excited to the state $|1\rangle$, leaving Q_0 in $|0\rangle$ to form a 'hole'. **C** and **D**, Experimental results showing particle (C) and hole (D) propagations under the initial conditions of **A** and **B**, respectively. **E** and **F**, Simulations of the particle and hole propagations, respectively. The agreement between the experimental results and the simulations demonstrates that the system can be accurately modeled by using an XY spin model. Furthermore, it confirms the precise synchronization of the operations across the qubits.

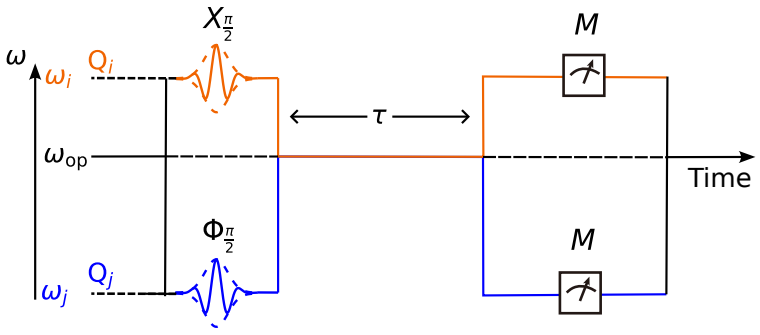

Figure S11: **Pulse sequence for calibrating the relative phase**. We rotate Q_i and Q_j to the XY plane and set the initial phase of Q_i as the reference. Then, we adjust the phase of Q_j, turn off the Z-pulse to let them resonantly couple for a time duration $\tau = \pi/4g_{ij}$, where g_{ij} is the coupling strength between Q_i and Q_j. At the end, we turn on the Z-pulse and perform the readout.

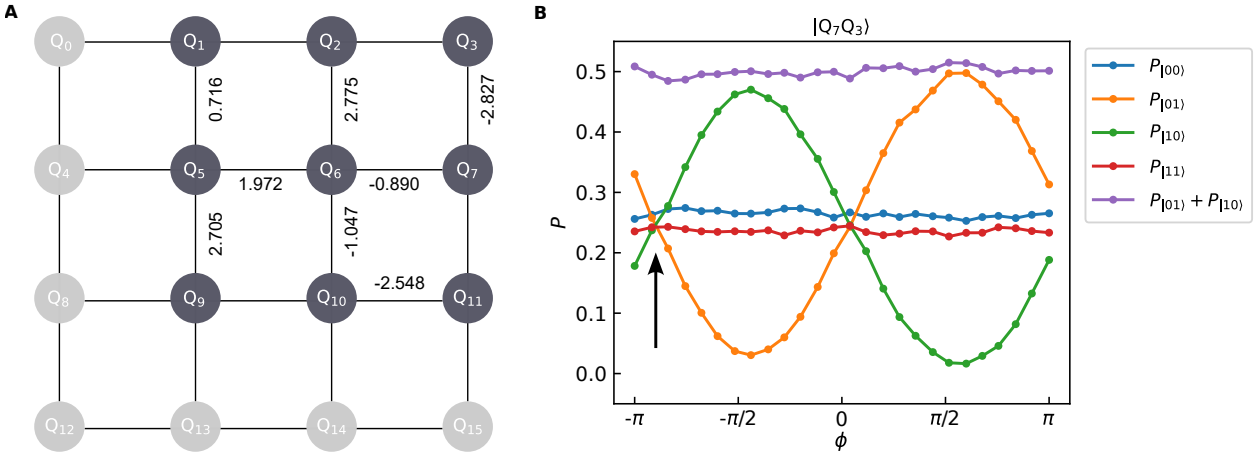

Figure S12: **Relative-phase calibration**. **A**, Relative-phase offsets (rad) between the adjacent qubits. **B**, Results of the experiments in Fig. S11. The position of the black arrow indicates the relative-phase offset between Q_3 and Q_7

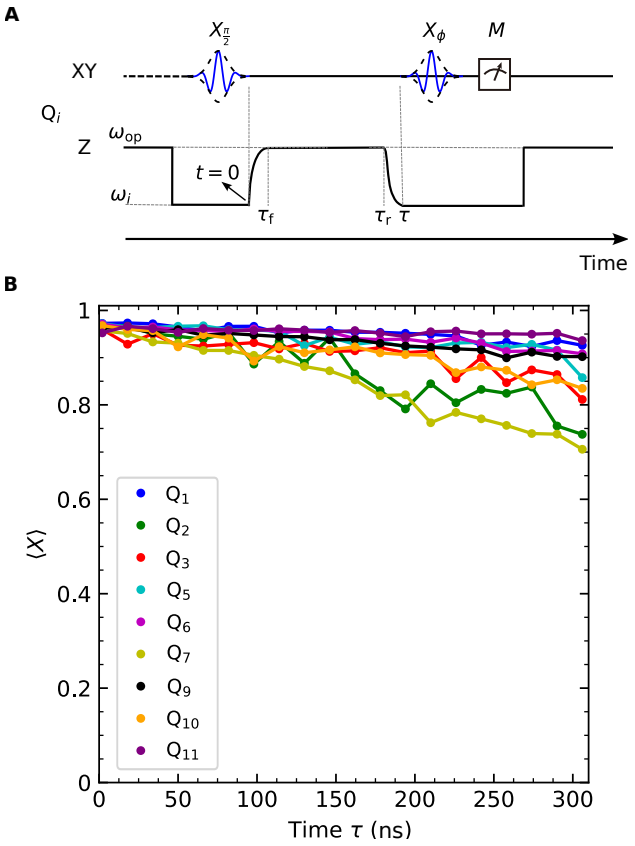

Figure S13: **Dynamical-phase calibration**. **A**, Pulse sequence to calibrate the accumulated dynamical phase during the Z-pulse control. **B**, Expectation values $\langle X \rangle$ after calibration for each qubit as a function of time τ.

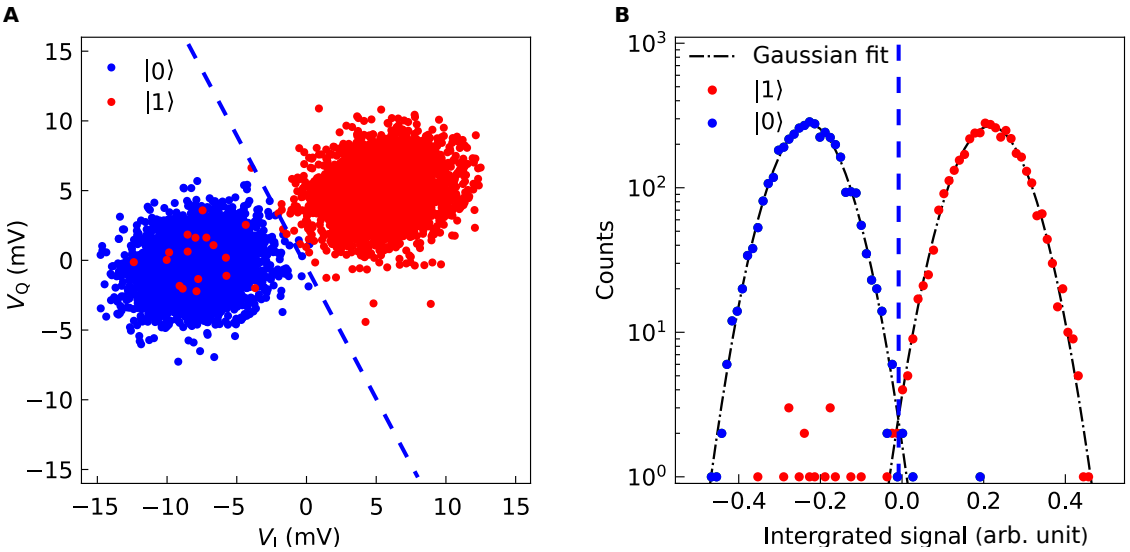

Figure S14: **Single-shot readout. A**, Time-integrated IQ signals of Q_{12} when all the sixteen qubits are prepared in state $|0\rangle^{\otimes 16}$ and in state $|1\rangle^{\otimes 16}$. **B**, Histograms of the data from **A**, showing data projected along the principal axis in the IQ plane. Dot-dashed lines represent Gaussian fits to the signal distributions for $|0\rangle$ and $|1\rangle$.

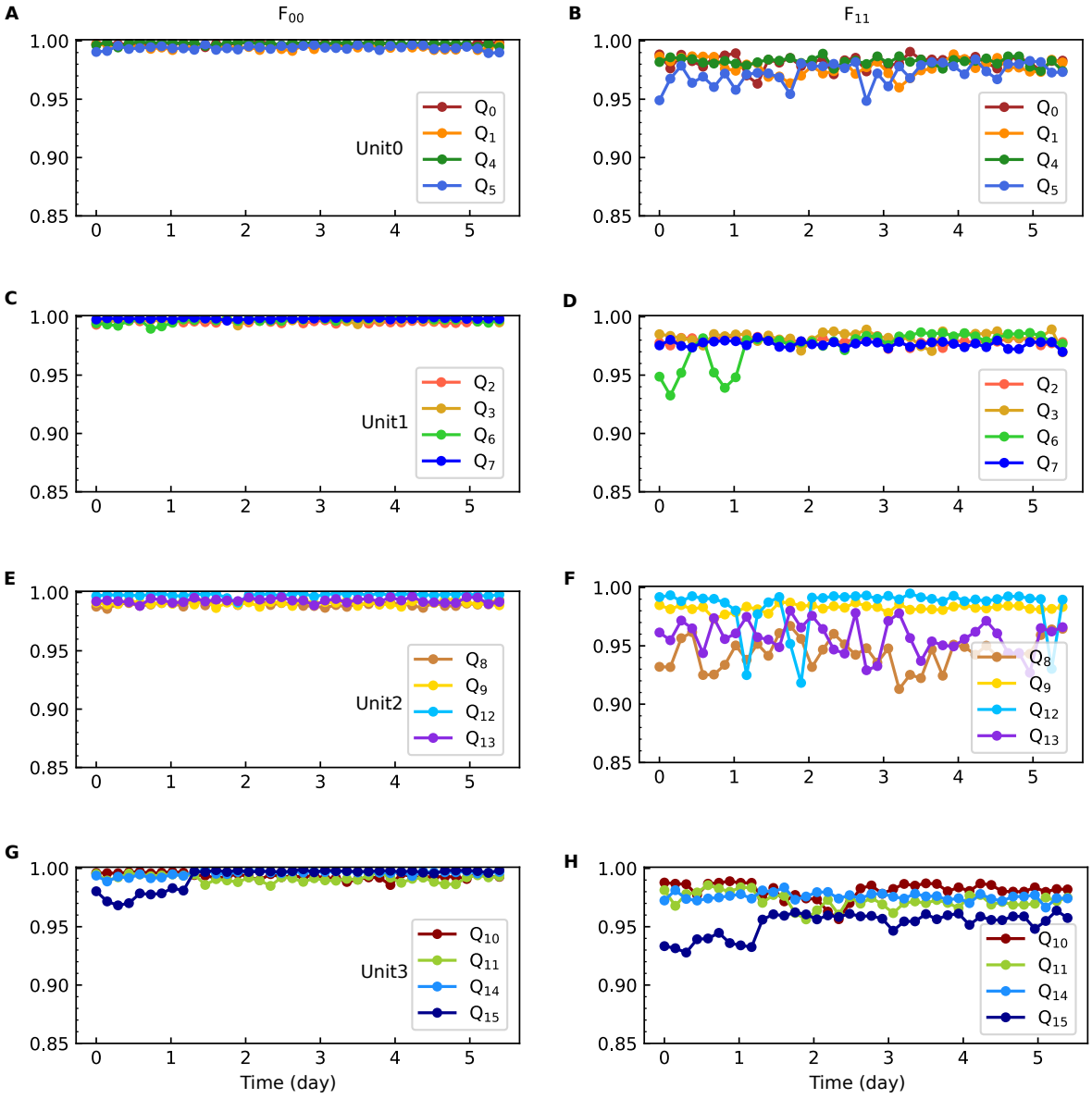

Figure S15: **Simultaneous readout fidelities F_{00} and F_{11}, of the 16 qubits in over five-day continuous measurement.**

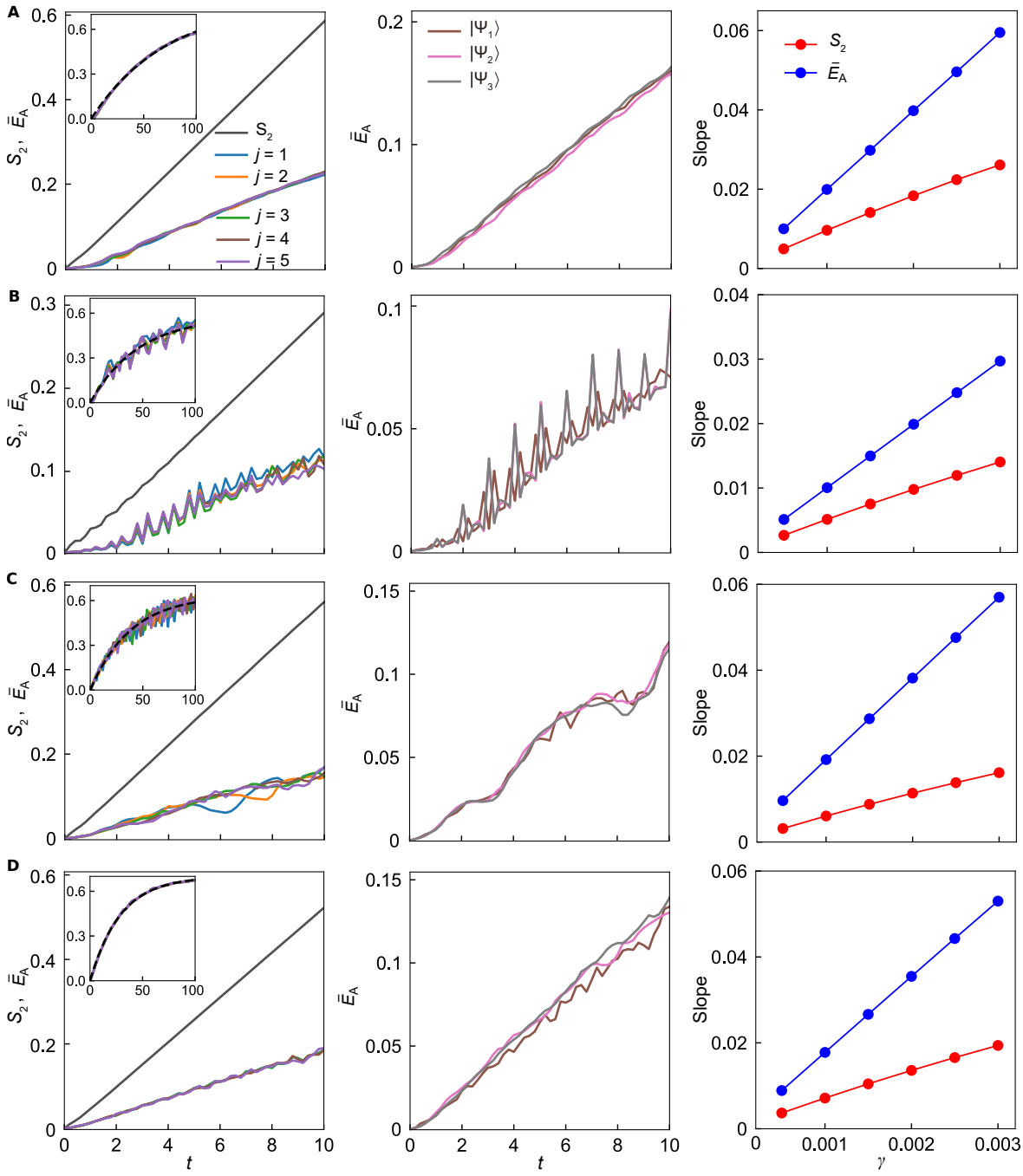

Figure S16: **Benchmark of many-body information leakage.** **a,** 1D mixed Ising model. **b,** Interacting Rydberg-atom Hamiltonian. **c**, 1D XY model. **d**, 2D XY model. (Left panel) Dynamics of S_2 and $\bar{E}_{\mathrm{A}}$, where we choose site j as subsystem A. The initial states are corresponding to $|\Psi_1\rangle$, and $\gamma = 0.002$. The insets show the long-time evolution of $\bar{E}_{\mathrm{A}}$, and the black dashed curves are fits according to Eq. (S25). (Middle panel) Dynamics of $\bar{E}_{\mathrm{A}}$ for different initial states with site 5 as subsystem A and $\gamma = 0.002$. (Right panel) Slopes of $S_2(t)$ and $\bar{E}_{\mathrm{A}}(t)$ in **a** versus the dissipation rate γ.

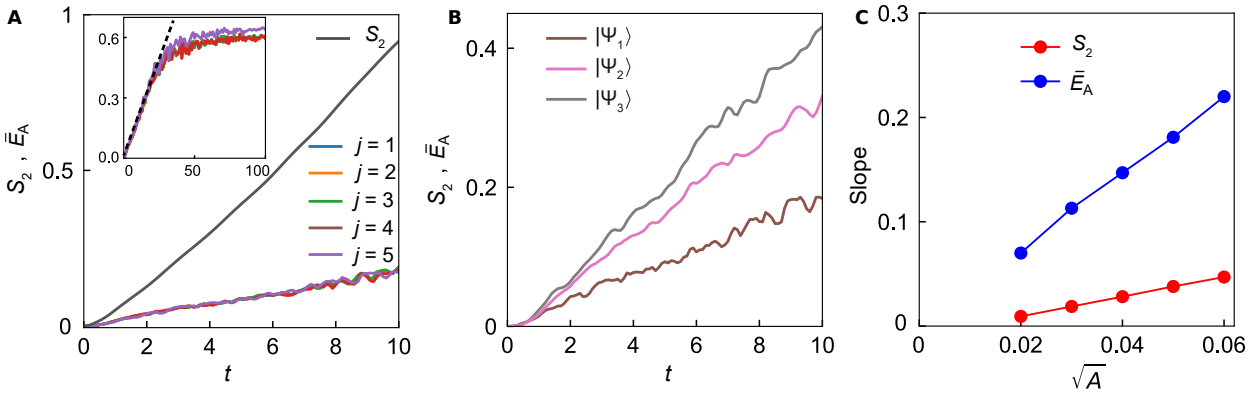

Figure S17: **Benchmark of many-body information leakage due to 1/f noise in the 2D XY model. a,** Dynamics of S_2 and $\bar{E}_{\mathrm{A}}$ under $1/f$ noise. We choose site j as subsystem A. The initial states are corresponding to $|\Psi_1\rangle$, and $\sqrt{A_j} = 0.03$. The insets are the long-time evolution of $\bar{E}_{\mathrm{A}}$, and the black dashed curve is a linear fit. **b,** Dynamics of $\bar{E}_{\mathrm{A}}$ for different initial states with site 5 as subsystem A and $\sqrt{A_j} = 0.03$. **c,** Slopes of $S_2(t)$ and $\bar{E}_{\mathrm{A}}(t)$ in **a** versus the noise intensity $\sqrt{A_j}$.

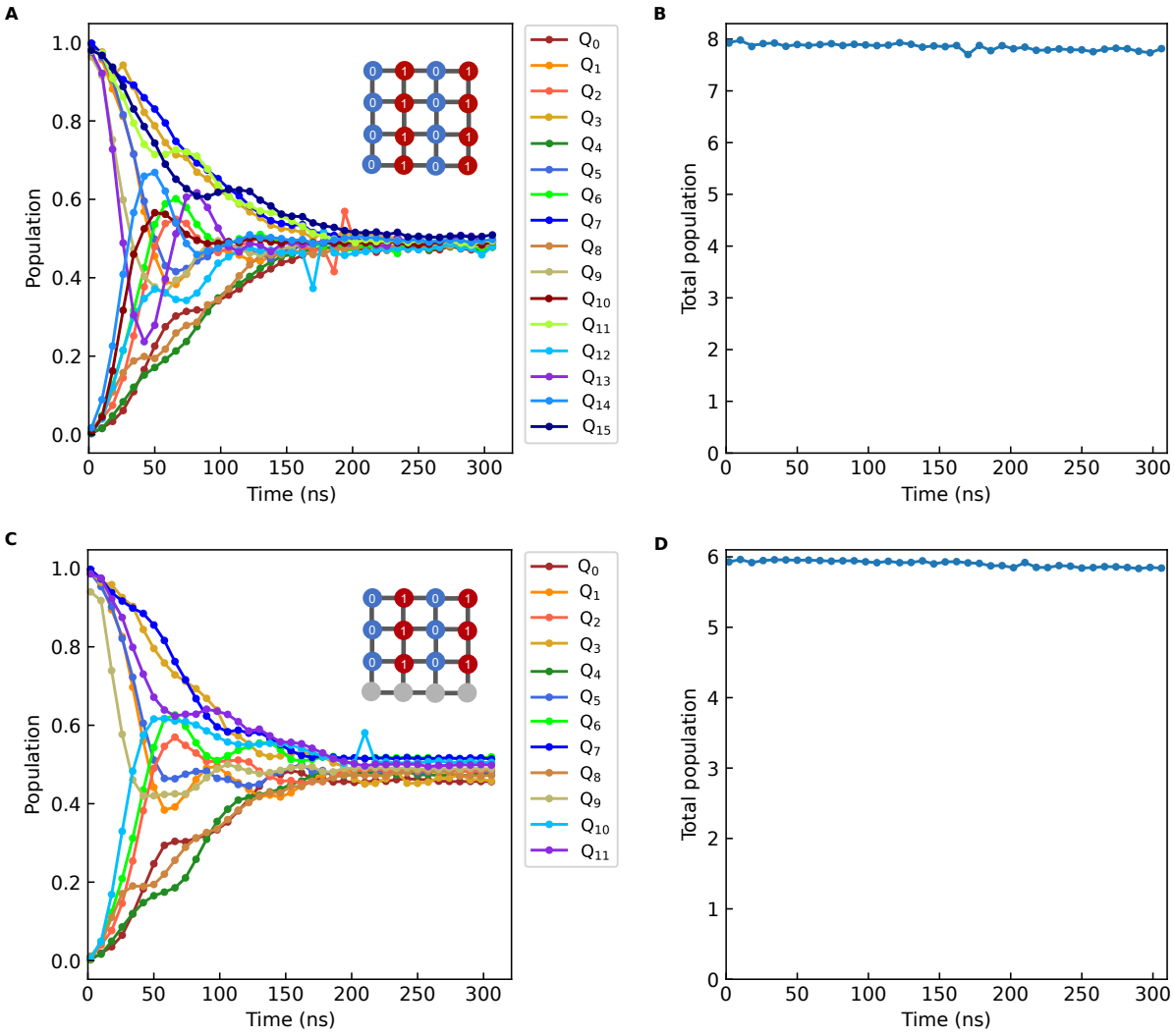

Figure S18: **Particle propagation.** **a**, Evolution of the Particles in the 16-qubit system with a half–filled initial state. **b**, Total-population evolution in **a**. **c**, Evolution of the particles in the 12-qubit system with a half-filled initial state. **d**, Total-populatoin evolution in **c**.

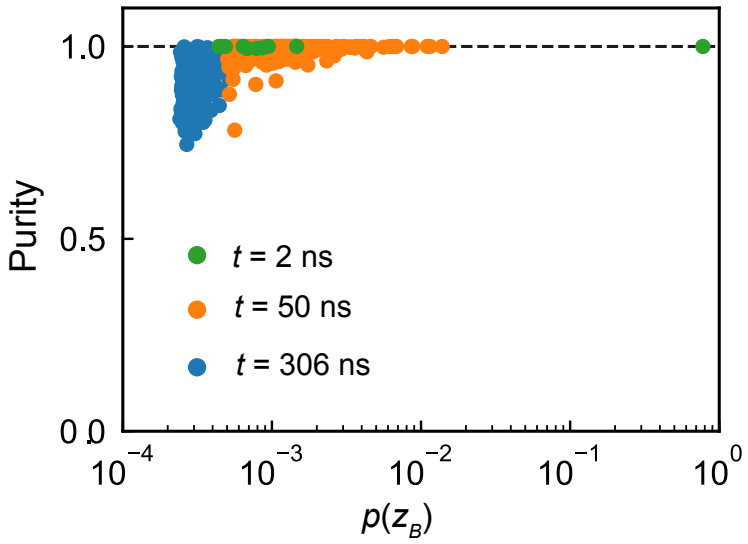

Figure S19: **Distributions of purity for each state $\tilde{\rho}_{\mathrm{A}}(\mathbf{z_B})$.** The purity of $\tilde{\rho}_{\mathrm{A}}(z_{\mathrm{B}})$ is defined as $\mathrm{Tr}\tilde{\rho}^2_{\mathrm{A}}(z_{\mathrm{B}})$.

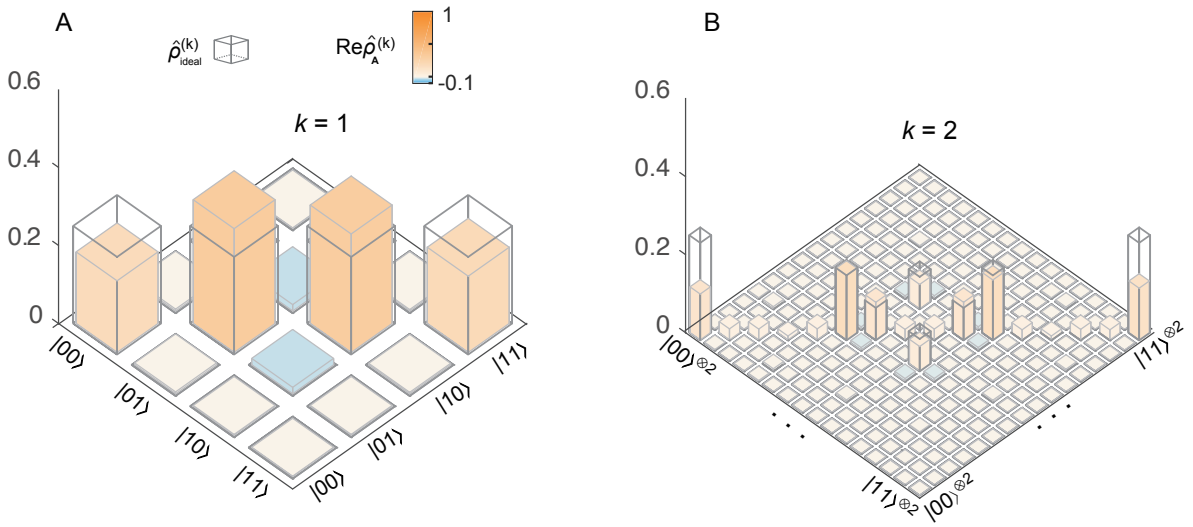

Figure S20: **Real parts of the density matrices $\hat{\rho}^{(\mathbf{k})}_{\mathbf{A}}$ without post-selection.** (**A, B**) Real parts of $\hat{\rho}^{(1)}_{\mathrm{A}}$ and $\hat{\rho}^{(2)}_{\mathrm{A}}$, respectively. The empty boxes indicate the corresponding ideal density matrices. For a half-filling state in a 16-qubit system, the ratio $\frac{p}{\mathcal{D}}|_{n(z_{\mathrm{B}})=7}$ is larger than $\frac{p}{\mathcal{D}}|_{n(z_{\mathrm{B}})=6} = \frac{p}{\mathcal{D}}|_{n(z_{\mathrm{B}})=8}$, where $n(z_{\mathrm{B}})$ denotes the total number of excitations in subsystem B, $\mathcal{D}|_{n(z_{\mathrm{B}})}$ is the Hilbert-space dimension of subsystem B for a fixed excitation number $n(z_{\mathrm{B}})$, and $p|_{n(z_{\mathrm{B}})}$ is the probability of measuring $n(z_{\mathrm{B}})$ excitations in subsystem B [$p|_{n(z_{\mathrm{B}})=7} = 1/2$, and $p|_{n(z_{\mathrm{B}})=6} = p|_{n(z_{\mathrm{B}})=8)} = 1/4$]. Consequently, in the experiment, more bit-strings with $n(z_{\mathrm{B}}) = 7$ were observed, leading to smaller measured probabilities for the $|00\rangle$ and $|11\rangle$ states of subsystem A compared with the ideal case.

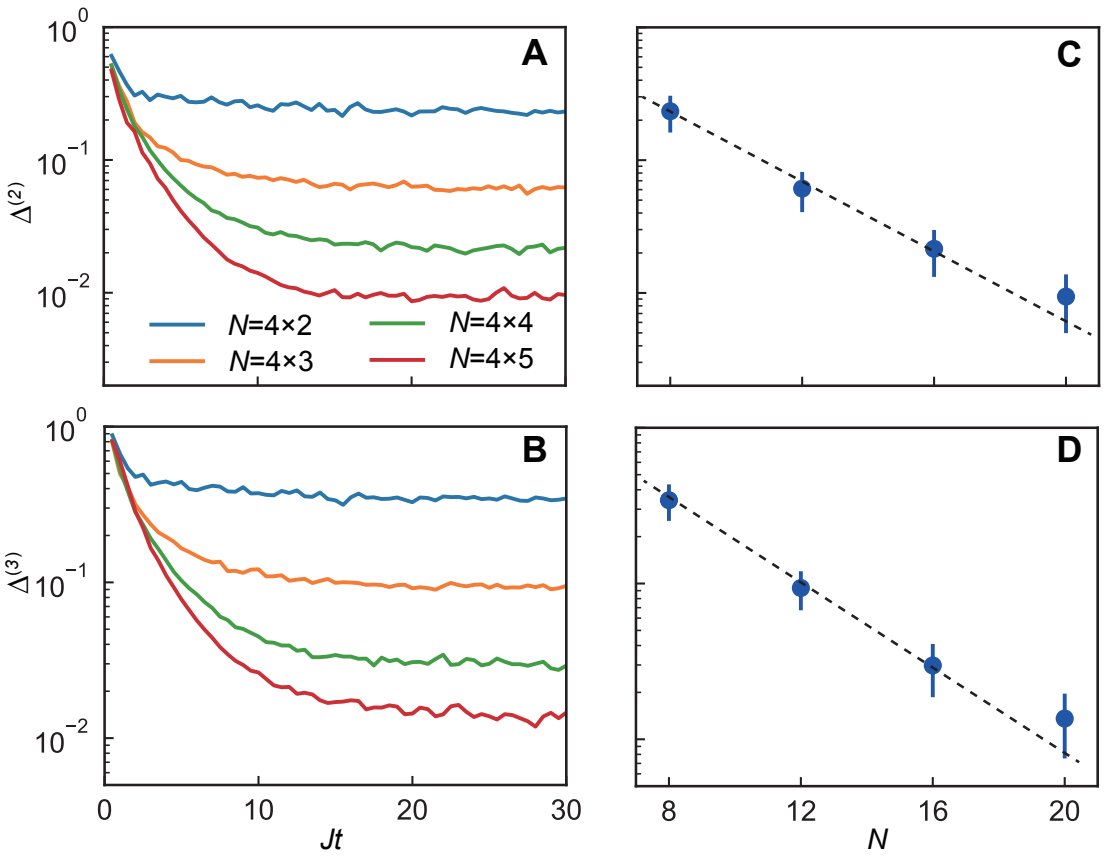

Figure S21: **Scaling of $\Delta^{(k)}$ for 2D XY model.** (**A, B**) Dynamics of $\Delta^{(2)}$ and $\Delta^{(3)}$ for different system sizes, respectively. (**C, D**) Saturated values of $\Delta^{(2)}$ and $\Delta^{(3)}$ versus the system size, respectively. The black dashed lines are exponential fits: $\Delta^{(k)} \sim e^{-N}$. To eliminate possible effects of symmetry, we introduce weak disorder and choose the initial states as random half-filling Fock states. The Hamiltonian is given by $\hat{H} = \sum_{\langle i,j \rangle} J(\hat{\sigma}_i^+ \hat{\sigma}_j^- + \text{h.c.}) + \sum_j h_j \hat{\sigma}_j^+ \hat{\sigma}_j^-$, where the on-site disorder h_j is uniformly sampled from the range $[0, J]$. The sampling numbers are 160, 80, 40, and 20 for system sizes: 4×2, 4×3, 4×4, and 4×5, respectively.

Movie S1.

Time evolution for the distributions of $\tilde{\rho}_{\mathrm{A}}(z_{\mathrm{B}})$ on the Bloch sphere.

PDF file S1.

The presentation slides of this work.

REFERENCES

1. A. Polkovnikov, K. Sengupta, A. Silva, M. Vengalattore, *Colloquium*: Nonequilibrium dynamics of closed interacting quantum systems. *Rev. Mod. Phys.* **83**, 863 (2011).

2. I. Buluta, F. Nori, Quantum simulators. *Science* **326**, 108–111 (2009).

3. A. Trabesinger, Quantum simulation. *Nat. Phys.* **8**, 263 (2012).

4. I. M. Georgescu, S. Ashhab, F. Nori, Quantum simulation. *Rev. Mod. Phys.* **86**, 153 (2014).

5. J. M. Deutsch, Quantum statistical mechanics in a closed system. *Phys. Rev. A* **43**, 2046–2049 (1991).

6. M. Srednicki, Chaos and quantum thermalization. *Phys. Rev. E* **50**, 888–901 (1994).

7. M. Srednicki, The approach to thermal equilibrium in quantized chaotic systems. *J. Phys. A Math. Gen.* **32**, 1163 (1999).

8. M. Rigol, V. Dunjko, M. Olshanii, Thermalization and its mechanism for generic isolated quantum systems. *Nature* **452**, 854–858 (2008).

9. C. Neill, P. Roushan, M. Fang, Y. Chen, M. Kolodrubetz, Z. Chen, A. Megrant, R. Barends, B. Campbell, B. Chiaro, A. Dunsworth, E. Jeffrey, J. Kelly, J. Mutus, P. J. J. O'Malley, C. Quintana, D. Sank, A. Vainsencher, J. Wenner, T. C. White, A. Polkovnikov, J. M. Martinis, Ergodic dynamics and thermalization in an isolated quantum system. *Nat. Phys.* **12**, 1037 (2016).

10. A. M. Kaufman, M. E. Tai, A. Lukin, M. Rispoli, R. Schittko, P. M. Preiss, M. Greiner, Quantum thermalization through entanglement in an isolated many-body system. *Science* **353**, 794–800 (2016).

11. L. D'Alessio, Y. Kafri, A. Polkovnikov, M. Rigol, From quantum chaos and eigenstate thermalization to statistical mechanics and thermodynamics. *Adv. Phys.* **65**, 239–362 (2016).

12. J. Choi, A. L. Shaw, I. S. Madjarov, X. Xie, R. Finkelstein, J. P. Covey, J. S. Cotler, D. K. Mark, H.-Y. Huang, A. Kale, H. Pichler, F. G. S. L. Brandão, S. Choi, M. Endres, Preparing random states and benchmarking with many-body quantum chaos. *Nature* **613**, 468–473 (2023).

13. W. W. Ho, S. Choi, Exact emergent quantum state designs from quantum chaotic dynamics. *Phys. Rev. Lett.* **128**, 060601 (2022).

14. J. S. Cotler, D. K. Mark, H.-Y. Huang, F. Hernández, J. Choi, A. L. Shaw, M. Endres, S. Choi, Emergent quantum state designs from individual many-body wave functions. *PRX Quantum* **4**, 010311 (2023).

15. D. K. Mark, F. Surace, A. Elben, A. L. Shaw, J. Choi, G. Refael, M. Endres, S. Choi, Maximum entropy principle in deep thermalization and in Hilbert-space ergodicity. *Phys. Rev. X* **14**, 041051 (2024).

16. J. M. Renes, R. Blume-Kohout, A. J. Scott, C. M. Caves, Symmetric informationally complete quantum measurements. *J. Math. Phys.* **45**, 2171–2180 (2004).

17. A. Ambainis, J. Emerson, in *Twenty-Second Annual IEEE Conference on Computational Complexity (CCC'07)* (IEEE, 2007), pp. 129–140.

18. D. V. Averin, K. Xu, Y. P. Zhong, C. Song, H. Wang, S. Han, Suppression of dephasing by qubit motion in superconducting circuits. *Phys. Rev. Lett.* **116**, 010501 (2016).

19. K. Xu, J.-J. Chen, Y. Zeng, Y.-R. Zhang, C. Song, W. Liu, Q. Guo, P. Zhang, D. Xu, H. Deng, K. Huang, H. Wang, X. Zhu, D. Zheng, H. Fan, Emulating many-body localization with a superconducting quantum processor. *Phys. Rev. Lett.* **120**, 050507 (2018).

20. T. Brydges, A. Elben, P. Jurcevic, B. Vermersch, C. Maier, B. P. Lanyon, P. Zoller, R. Blatt, C. F. Roos, Probing Rényi entanglement entropy via randomized measurements. *Science* **364**, 260–263 (2019).

21. Google Quantum AI and Collaborators, Measurement-induced entanglement and teleportation on a noisy quantum processor. *Nature* **622**, 481–486 (2023).

22. A. H. Karamlou, I. T. Rosen, S. E. Muschinske, C. N. Barrett, A. Di Paolo, L. Ding, P. M. Harrington, M. Hays, R. Das, D. K. Kim, B. M. Niedzielski, M. Schuldt, K. Serniak, M. E. Schwartz, J. L. Yoder, S. Gustavsson, Y. Yanay, J. A. Grover, W. D. Oliver, Probing entanglement in a 2D hard-core Bose-Hubbard lattice. *Nature* **629**, 561–566 (2024).

23. J. Béjanin, T. McConkey, J. Rinehart, C. Earnest, C. McRae, D. Shiri, J. Bateman, Y. Rohanizadegan, B. Penava, P. Breul, S. Royak, M. Zapatka, A. G. Fowler, M. Mariantoni, Three-dimensional wiring for extensible quantum computing: The quantum socket. *Phys. Rev. Appl.* **6**, 044010 (2016).

24. J. Rahamim, T. Behrle, M. Peterer, A. Patterson, P. Spring, T. Tsunoda, R. Manenti, G. Tancredi, P. Leek, Double-sided coaxial circuit QED with out-of-plane wiring. *Appl. Phys. Lett.* **110**, 222602 (2017).

25. D. Rosenberg, D. Kim, R. Das, D. Yost, S. Gustavsson, D. Hover, P. Krantz, A. Melville, L. Racz, G. Samach, S. J. Weber, F. Yan, J. L. Yoder, A. J. Kerman, W. D. Oliver, 3D integrated superconducting qubits. *npj Quantum Inf.* **3**, 42 (2017).

26. D.-R. W. Yost, M. E. Schwartz, J. Mallek, D. Rosenberg, C. Stull, J. L. Yoder, G. Calusine, M. Cook, R. Das, A. L. Day, E. B. Golden, D. K. Kim, A. Melville, B. M. Niedzielski, W. Woods, A. J. Kerman, W. D. Oliver, Solid-state qubits integrated with superconducting through-silicon vias. *npj Quantum Inf.* **6**, 59 (2020).

27. P. A. Spring, S. Cao, T. Tsunoda, G. Campanaro, S. Fasciati, J. Wills, M. Bakr, V. Chidambaram, B. Shteynas, L. Carpenter, P. Gow, J. Gates, B. Vlastakis, P. J. Leek, High coherence and low cross-talk in a tileable 3D integrated superconducting circuit architecture. *Sci. Adv.* **8**, eabl6698 (2022).

28. J. Koch, T. M. Yu, J. Gambetta, A. A. Houck, D. I. Schuster, J. Majer, A. Blais, M. H. Devoret, S. M. Girvin, R. J. Schoelkopf, Charge-insensitive qubit design derived from the Cooper pair box. *Phys. Rev. A* **76**, 042319 (2007).

29. M. Kjaergaard, M. E. Schwartz, J. Braumüller, P. Krantz, J. I.-J. Wang, S. Gustavsson, W. D. Oliver, Superconducting qubits: Current state of play. *Annu. Rev. Condens. Matter Phys.* **11**, 369–395 (2020).

30. I. Siddiqi, Engineering high-coherence superconducting qubits. *Nat. Rev. Mater.* **6**, 875–891 (2021).

31. P. Roushan, C. Neill, J. Tangpanitanon, V. M. Bastidas, A. Megrant, R. Barends, Y. Chen, Z. Chen, B. Chiaro, A. Dunsworth, A. Fowler, B. Foxen, M. Giustina, E. Jeffrey, J. Kelly, E. Lucero, J. Mutus, M. Neeley, C. Quintana, D. Sank, A. Vainsencher, J. Wenner, T. White, H. Neven, D. G. Angelakis, J. Martinis, Spectroscopic signatures of localization with interacting photons in superconducting qubits. *Science* **358**, 1175–1179 (2017).

32. Z. Yan, Y.-R. Zhang, M. Gong, Y. Wu, Y. Zheng, S. Li, C. Wang, F. Liang, J. Lin, Y. Xu, C. Guo, L. Sun, C. Z. Peng, K. Xia, H. Deng, H. Rong, J. Q. You, F. Nori, H. Fan, X. Zhu, J. W. Pan, Strongly correlated quantum walks with a 12-qubit superconducting processor. *Science* **364**, 753–756 (2019).

33. Y. Ye, Z.-Y. Ge, Y. Wu, S. Wang, M. Gong, Y.-R. Zhang, Q. Zhu, R. Yang, S. Li, F. Liang, J. Lin, Y. Xu, C. Guo, L. Sun, C. Cheng, N. Ma, Z. Y. Meng, H. Deng, H. Rong, C.-Y. Lu, C.-Z. Peng, H. Fan, X. Zhu, J.-W. Pan, Propagation and localization of collective excitations on a 24-qubit superconducting processor. *Phys. Rev. Lett.* **123**, 050502 (2019).

34. T. I. Andersen, N. Astrakhantsev, A. H. Karamlou, J. Berndtsson, J. Motruk, A. Szasz, J. A. Gross, A. Schuckert, T. Westerhout, Y. Zhang, E. Forati, D. Rossi, B. Kobrin, A. D. Paolo, A. R. Klots, I. Drozdov, V. Kurilovich, A. Petukhov, L. B. Ioffe, A. Elben, A. Rath, V. Vitale, B. Vermersch, R. Acharya, L. A. Beni, K. Anderson, M. Ansmann, F. Arute, K. Arya, A. Asfaw, J. Atalaya, B. Ballard, J. C. Bardin, A. Bengtsson, A. Bilmes, G. Bortoli, A. Bourassa, J. Bovaird, L. Brill, M. Broughton, D. A. Browne, B. Buchea, B. B. Buckley, D. A. Buell, T. Burger, B. Burkett, N. Bushnell, A. Cabrera, J. Campero, H. S. Chang, Z. Chen, B. Chiaro, J. Claes, A. Y. Cleland, J. Cogan, R. Collins, P. Conner, W. Courtney, A. L. Crook, S. das, D. M. Debroy, L. Lorenzo, A. D. T. Barba, S. Demura, P. Donohoe, A. Dunsworth, C. Earle, A. Eickbusch, A. M. Elbag, M. Elzouka, C. Erickson, L. Faoro, R. Fatemi, V. S. Ferreira, L. F. Burgos, A. G. Fowler, B. Foxen, S. Ganjam, R. Gasca, W. Giang, C. Gidney, D. Gilboa, M.

Giustina, R. Gosula, A. G. Dau, D. Graumann, A. Greene, S. Habegger, M. C. Hamilton, M. Hansen, M. P. Harrigan, S. D. Harrington, S. Heslin, P. Heu, G. Hill, M. R. Hoffmann, H. Y. Huang, T. Huang, A. Huff, W. J. Huggins, S. V. Isakov, E. Jeffrey, Z. Jiang, C. Jones, S. Jordan, C. Joshi, P. Juhas, D. Kafri, H. Kang, K. Kechedzhi, T. Khaire, T. Khattar, M. Khezri, M. Kieferová, S. Kim, A. Kitaev, P. Klimov, A. N. Korotkov, F. Kostritsa, J. M. Kreikebaum, D. Landhuis, B. W. Langley, P. Laptev, K. M. Lau, L. L. Guevel, J. Ledford, J. Lee, K. W. Lee, Y. D. Lensky, B. J. Lester, W. Y. Li, A. T. Lill, W. Liu, W. P. Livingston, A. Locharla, D. Lundahl, A. Lunt, S. Madhuk, A. Maloney, S. Mandrà, L. S. Martin, O. Martin, S. Martin, C. Maxfield, J. McClean, M. McEwen, S. Meeks, K. C. Miao, A. Mieszala, S. Molina, S. Montazeri, A. Morvan, R. Movassagh, C. Neill, A. Nersisyan, M. Newman, A. Nguyen, M. Nguyen, C. H. Ni, M. Y. Niu, W. D. Oliver, K. Ottosson, A. Pizzuto, R. Potter, O. Pritchard, L. P. Pryadko, C. Quintana, M. J. Reagor, D. M. Rhodes, G. Roberts, C. Rocque, E. Rosenberg, N. C. Rubin, N. Saei, K. Sankaragomathi, K. J. Satzinger, H. F. Schurkus, C. Schuster, M. J. Shearn, A. Shorter, N. Shutty, V. Shvarts, V. Sivak, J. Skruzny, S. Small, W. C. Smith, S. Springer, G. Sterling, J. Suchard, M. Szalay, A. Sztein, D. Thor, A. Torres, M. M. Torunbalci, A. Vaishnav, S. Vdovichev, B. Villalonga, C. V. Heidweiller, S. Waltman, S. X. Wang, T. White, K. Wong, B. W. K. Woo, C. Xing, Z. J. Yao, P. Yeh, B. Ying, J. Yoo, N. Yosri, G. Young, A. Zalcman, N. Zhu, N. Zobrist, H. Neven, R. Babbush, S. Boixo, J. Hilton, E. Lucero, A. Megrant, J. Kelly, Y. Chen, V. Smelyanskiy, G. Vidal, P. Roushan, A. M. Läuchli, D. A. Abanin, X. Mi, Thermalization and criticality on an analogue-digital quantum simulator. *Nature* **638**, 79–85 (2025).

35. B. Blain, G. Marchegiani, L. Amico, G. Catelani, Suppressing chaos with mixed superconducting-qubit devices. *Phys. Rev. Appl.* **24**, 014048 (2025).

36. C. E. Porter, R. G. Thomas, Fluctuations of nuclear reaction widths. *Phys. Rev.* **104**, 483 (1956).

37. F. Arute, K. Arya, R. Babbush, D. Bacon, J. C. Bardin, R. Barends, R. Biswas, S. Boixo, F. G. S. L. Brandao, D. A. Buell, B. Burkett, Y. Chen, Z. Chen, B. Chiaro, R. Collins, W. Courtney, A. Dunsworth, E. Farhi, B. Foxen, A. Fowler, C. Gidney, M. Giustina, R. Graff, K. Guerin, S. Habegger, M. P. Harrigan, M. J. Hartmann, A. Ho, M. Hoffmann, T. Huang, T. S. Humble, S. V. Isakov, E. Jeffrey, Z. Jiang, D. Kafri, K. Kechedzhi, J. Kelly, P. V. Klimov, S.

Knysh, A. Korotkov, F. Kostritsa, D. Landhuis, M. Lindmark, E. Lucero, D. Lyakh, S. Mandra, J. R. McClean, M. McEwen, A. Megrant, X. Mi, K. Michielsen, M. Mohseni, J. Mutus, O. Naaman, M. Neeley, C. Neill, M. Y. Niu, E. Ostby, A. Petukhov, J. C. Platt, C. Quintana, E. G. Rieffel, P. Roushan, N. C. Rubin, D. Sank, K. J. Satzinger, V. Smelyanskiy, K. J. Sung, M. D. Trevithick, A. Vainsencher, B. Villalonga, T. White, Z. J. Yao, P. Yeh, A. Zalcman, H. Neven, J. M. Martinis, Quantum supremacy using a programmable superconducting processor. *Nature* **574**, 505–510 (2019).

38. T. Liu, S. Liu, H. Li, H. Li, K. Huang, Z. Xiang, X. Song, K. Xu, D. Zheng, H. Fan, Observation of entanglement transition of pseudo-random mixed states. *Nat. Commun.* **14**, 1971 (2023).

39. D. A. Lidar, Lecture notes on the theory of open quantum systems. arXiv:1902.00967 [quant-ph] (2019).

40. E. Paladino, Y. M. Galperin, G. Falci, B. L. Altshuler, 1/*f* noise: Implications for solid-state quantum information. *Rev. Mod. Phys.* **86**, 361 (2014).

41. F. Yoshihara, K. Harrabi, A. O. Niskanen, Y. Nakamura, J. S. Tsai, Decoherence of flux qubits due to 1/*f* flux noise. *Phys. Rev. Lett.* **97**, 167001 (2006).

42. R. McDermott, Materials origins of decoherence in superconducting qubits. *IEEE Trans. Appl. Supercond.* **19**, 2–13 (2009).

43. A. Kitaev, J. Preskill, Topological entanglement entropy. *Phys. Rev. Lett.* **96**, 110404 (2006).

44. X. Chen, Z.-C. Gu, X.-G. Wen, Local unitary transformation, long-range quantum entanglement, wave function renormalization, and topological order. *Phys. Rev. B* **82**, 155138 (2010).

45. Z.-Y. Ge, F. Nori, Identifying entanglement phases with bipartite projected ensembles. *Phys. Rev. Res.* **7**, 043022 (2025).

46. H.-P. Breuer, E.-M. Laine, J. Piilo, B. Vacchini, *Colloquium*: Non-Markovian dynamics in open quantum systems. *Rev. Mod. Phys.* **88**, 021002 (2016).

47. A. Rivas, S. F. Huelga, M. B. Plenio, Entanglement and non-markovianity of quantum evolutions. *Phys. Rev. Lett.* **105**, 050403 (2010).

48. X.-M. Lu, X. Wang, C. P. Sun, Quantum Fisher information flow and non-Markovian processes of open systems. *Phys. Rev. A* **82**, 042103 (2010).

49. Y.-N. Lu, Y.-R. Zhang, G.-Q. Liu, F. Nori, H. Fan, X.-Y. Pan, Observing information backflow from controllable non-Markovian multichannels in diamond. *Phys. Rev. Lett.* **124**, 210502 (2020).

50. C. Wang, C. Axline, Y. Y. Gao, T. Brecht, Y. Chu, L. Frunzio, M. Devoret, R. J. Schoelkopf, Surface participation and dielectric loss in superconducting qubits. *Appl. Phys. Lett.* **107**, 162601 (2015).

51. E. Jeffrey, D. Sank, J. Mutus, T. White, J. Kelly, R. Barends, Y. Chen, Z. Chen, B. Chiaro, A. Dunsworth, A. Megrant, P. J. O'Malley, C. Neill, P. Roushan, A. Vainsencher, J. Wenner, A. N. Cleland, J. M. Martinis, Fast accurate state measurement with superconducting qubits. *Phys. Rev. Lett.* **112**, 190504 (2014).

52. Y. Zheng, C. Song, M.-C. Chen, B. Xia, W. Liu, Q. Guo, L. Zhang, D. Xu, H. Deng, K. Huang, Y. Wu, Z. Yan, D. Zheng, L. Lu, J.-W. Pan, H. Wang, C.-Y. Lu, X. Zhu, Solving systems of linear equations with a superconducting quantum processor. *Phys. Rev. Lett.* **118**, 210504 (2017).

53. J. Johansson, P. Nation, F. Nori, QuTiP 2: A Python framework for the dynamics of open quantum systems. *Comput. Phys. Commun.* **184**, 1234–1240 (2013).

54. T. Roy, S. Kundu, M. Chand, A. Vadiraj, A. Ranadive, N. Nehra, M. P. Patankar, J. Aumentado, A. Clerk, R. Vijay, Broadband parametric amplification with impedance engineering: Beyond the gain-bandwidth product. *Appl. Phys. Lett.* **107**, 262601 (2015).

55. J. Braumüller, L. Ding, A. P. Vepsäläinen, Y. Sung, M. Kjaergaard, T. Menke, R. Winik, D. Kim, B. M. Niedzielski, A. Melville, J. L. Yoder, C. F. Hirjibehedin, T. P. Orlando, S.

Gustavsson, W. D. Oliver, Characterizing and optimizing qubit coherence based on SQUID geometry. *Phys. Rev. Appl.* **13**, 054079 (2020).

56. S. Bravyi, D. P. DiVincenzo, D. Loss, Schrieffer–Wolff transformation for quantum many-body systems. *Ann. Phys.* **326**, 2793–2826 (2011).

57. A. Potts, P. Routley, G. J. Parker, J. Baumberg, P. De Groot, Novel fabrication methods for submicrometer Josephson junction qubits. *J. Mater. Sci. Mater. Electron.* **12**, 289–293 (2001).

58. L. DiCarlo, J. M. Chow, J. M. Gambetta, L. S. Bishop, B. R. Johnson, D. Schuster, J. Majer, A. Blais, L. Frunzio, S. Girvin, R. J. Schoelkopf, Demonstration of two-qubit algorithms with a superconducting quantum processor. *Nature* **460**, 240–244 (2009).

59. E. Magesan, J. M. Gambetta, J. Emerson, Scalable and robust randomized benchmarking of quantum processes. *Phys. Rev. Lett.* **106**, 180504 (2011).

60. J. M. Gambetta, A. D. Córcoles, S. T. Merkel, B. R. Johnson, J. A. Smolin, J. M. Chow, C. A. Ryan, C. Rigetti, S. Poletto, T. A. Ohki, M. B. Ketchen, M. Steffen, Characterization of addressability by simultaneous randomized benchmarking. *Phys. Rev. Lett.* **109**, 240504 (2012).

61. R. Barends, J. Kelly, A. Megrant, A. Veitia, D. Sank, E. Jeffrey, T. C. White, J. Mutus, A. G. Fowler, B. Campbell, Y. Chen, Z. Chen, B. Chiaro, A. Dunsworth, C. Neill, P. O'Malley, P. Roushan, A. Vainsencher, J. Wenner, A. N. Korotkov, A. N. Cleland, J. M. Martinis, Superconducting quantum circuits at the surface code threshold for fault tolerance. *Nature* **508**, 500–503 (2014).

62. E. A. Sete, J. M. Martinis, A. N. Korotkov, Quantum theory of a bandpass Purcell filter for qubit readout. *Phys. Rev. Appl.* **92**, 012325 (2015).

63. J. Gambetta, A. Blais, M. Boissonneault, A. A. Houck, D. Schuster, S. M. Girvin, Quantum trajectory approach to circuit QED: Quantum jumps and the Zeno effect. *Phys. Rev. A* **77**, 012112 (2008).

64. X. Jin, A. Kamal, A. Sears, T. Gudmundsen, D. Hover, J. Miloshi, R. Slattery, F. Yan, J. Yoder, T. Orlando, S. Gustavsson, W. D. Oliver, Thermal and residual excited-state population in a 3D transmon qubit. *Phys. Rev. Lett.* **114**, 240501 (2015).

65. M. A. Rol, L. Ciorciaro, F. K. Malinowski, B. M. Tarasinski, R. E. Sagastizabal, C. C. Bultink, Y. Salathe, N. Haandbæk, J. Sedivy, L. DiCarlo, Time-domain characterization and correction of on-chip distortion of control pulses in a quantum processor. *Appl. Phys. Lett.* **116**, 054001 (2020).

66. P. Klimov, J. Kelly, Z. Chen, M. Neeley, A. Megrant, B. Burkett, R. Barends, K. Arya, B. Chiaro, Y. Chen, A. Dunsworth, A. Fowler, B. Foxen, C. Gidney, M. Giustina, R. Graff, T. Huang, E. Jeffrey, E. Lucero, J. Y. Mutus, O. Naaman, C. Neill, C. Quintana, P. Roushan, D. Sank, A. Vainsencher, J. Wenner, T. C. White, S. Boixo, R. Babbush, V. N. Smelyanskiy, H. Neven, J. M. Martinis, Fluctuations of energy-relaxation times in superconducting qubits. *Phys. Rev. Lett.* **121**, 090502 (2018).

67. J. J. Burnett, A. Bengtsson, M. Scigliuzzo, D. Niepce, M. Kudra, P. Delsing, J. Bylander, Decoherence benchmarking of superconducting qubits. *npj Quantum Inf.* **5**, 54 (2019).

68. X.-Y. Guo, Z.-Y. Ge, H. Li, Z. Wang, Y.-R. Zhang, P. Song, Z. Xiang, X. Song, Y. Jin, L. Lu, K. Xu, D. Zheng, H. Fan, Observation of Bloch oscillations and Wannier-Stark localization on a superconducting quantum processor. *npj Quantum Inf.* **7**, 51 (2021).